

Analysis Note:

Anti-flow of Kaon in Au+Au Collisions at

$$\sqrt{s_{NN}} = 3 - 3.9 \text{ GeV}$$

Zuowen Liu, Li-ke Liu, Xing Wu, Guoping Wang

Abstract

In this note, we present the measurement of anti-flow of kaons in Au+Au collisions at $\sqrt{s_{NN}} = 3.0, 3.2, 3.5, 3.9$ GeV with the STAR experiment under its fixed target configuration at RHIC. Directed flow of π^\pm, K^\pm, K_S^0, p , and Λ are presented in different centrality, transverse momentum, and rapidity intervals. π^+, K^\pm , and K_S^0 show anti-flow at low p_T ($p_T < 0.6$ GeV/c) at $\sqrt{s_{NN}} = 3.0, 3.2, 3.5, 3.9$ GeV. And the result have been compared with JAM model. The data-model comparison indicates that anti-flow of kaons at low p_T could be explained by shadowing effect from spectator.

CONTENTS

1. Analysis setup	4
1.1. Introduction of FXT	4
1.2. Dataset and event selection	5
1.3. Badrun rejection and centrality determination	5
1.4. Basic track selection	6
2. Analysis method	6
2.1. Event plane reconstruction	6
2.1.1. Recentering correction	7
2.1.2. Shifting correction	8
2.1.3. Event plane resolution	8
2.2. Particle identification	10
2.2.1. π , K, p identification	10
2.2.2. K_S^0 , Λ identification	12
2.3. Efficiency correction	14
3. Results	17
3.1. Directed flow of π , K, p	17
3.1.1. Rapidity dependence of v_1	17
3.1.2. Transverse momentum dependence of $v_1(y)$	18
3.1.3. Systematic uncertainty	20
3.2. Directed flow of K_S^0 , Λ	21
3.2.1. Rapidity dependence of v_1	24
3.2.2. Transverse momentum dependence of $v_1(y)$	24
3.2.3. Systematic uncertainty	25
4. Summary	27
A. Appendix	32
B. PID cuts and acceptance plots	32
C. v_1 plots for other energies	32

1. ANALYSIS SETUP

This section shows the setup of analysis. The first part of this section introduces STAR Fixed Target(FXT) mode. Second one is dataset and event selection used in the analysis. At last, bad-run rejection and centrality determination are discussed.

1.1. Introduction of FXT

There are two modes at RHIC-STAR, Fixed Target (FXT) mode and Collider mode. FXT mode of STAR covers center of mass energy ($\sqrt{s_{NN}}$) from 3 to 13.7 GeV, which extends the flow measurement to lower collision energy. In this way, FXT mode could reach higher baryon density region ($\mu_B = 750$ MeV at most). To achieve this goal, One piece of gold foil is fixed at the end of Time Projection Chamber (TPC)[1] as target. And the projectile which is accelerated gold beam would collide with it. Fig. 1 shows the schematic plot for fixed target mode.

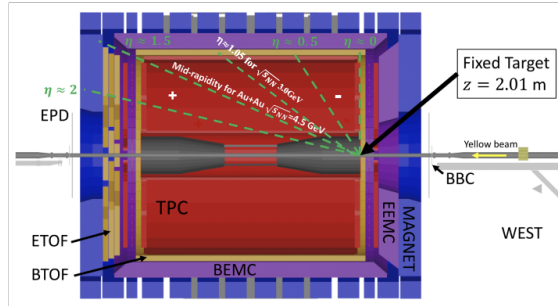


FIG. 1. The schematic plot of Fixed Target mode at STAR.

The laboratory system should be transferred to the Center of Mass System (CMS), if one want to analysis physical observation conveniently. According to the Lorentz transformation, Rapidity (y) of the final state particle in the Center of Mass System could be calculated as equation 1, where y_{lab} is rapidity of emitted particle in the laboratory frame, y_{beam} is rapidity of gold beam in the CMS. And we would discuss flow measurement in the Center of Mass System as follows.

$$y_{CMS} = y_{lab} - y_{beam} \quad (1)$$

TABLE I. Dataset and event cuts for $\sqrt{s_{NN}} = 3, 3.2, 3.5, 3.9$ GeV.

$\sqrt{s_{NN}}$ (GeV)	production tag	library tag	trigger ID	Vz(cm)	Vr (cm)
3.0	P19ic	SL20d	620052	[198, 202]	2
3.2	P23id	SL23d	680001	[198, 202]	2
3.5	P23ie	SL23e	720000	[198, 202]	2
3.9	P23ie	SL23e	730000	[198, 202]	2

1.2. Dataset and event selection

In this analysis, four collision energies ($\sqrt{s_{NN}} = 3, 3.2, 3.5, 3.9$ GeV) from fixed target mode are involved. The events from minimum bias trigger are selected. Vertex cut in the X and Y direction is applied to exclude the events colliding with beam pipe, and vertex cut along the Z direction ensure that selection events are from collision on the gold foil. The detailed triggers and vertex cuts are summarized in the TABLE. I.

1.3. Badrun rejection and centrality determination

Data production at STAR is run-by-run type, and the data is tagged with different run numbers. Run-by-run QA is necessary to reject the bad runs, which may caused by the broken detector etc. This job was finished by STAR QA group, and the bad-run list used in this analysis could be found at the [summary page](#) from QA group.

Moreover, the centrality determination work is vital in Heavy Ion Collision. Glauber Monte Carlo (MC) simulation [2] is applied to describe the reference multiplicity distribution, which is corrected by pile-up rejection and luminosity correction etc. The number of participant particle (N_{part}) and the number of collision particles (N_{coll}) can be extracted by the formula 2 in MC model.

$$\frac{dN_{ch}}{d\eta} = n_{pp} \left[(1 - x) \frac{N_{part}}{2} + x N_{coll} \right] \quad (2)$$

This work is finished by STAR Centrality group, a class([StRefMultCorr](#)) is provided. One can call the class and get the refMult cut.

Track cuts
nHitsFit > 15
DCA < 3 cm

TABLE II. The basic track cuts

1.4. Basic track selection

The basic track cuts can assure every track used in the analysis meet the minimum experimental requirements. For example, the $n\text{HitsFit} > 15$ cut requires that the track passing TPC have fifteen fitting hits at least, which could reduce the track merging effect (two tracks are merged as one.). The total basic track cuts are summarized at TABLE II.

2. ANALYSIS METHOD

In this section, event plane reconstruction would be described firstly. Second part is identification for measured particles, including identified particles(π^+ and π^-), and weak decay particles(K_0^S and Λ). Last one is efficiency correction, including TPC tracking efficiency, TOF matching efficiency and particle reconstruction efficiency.

2.1. Event plane reconstruction

Event plane method is one of common method in the anisotropic flow analysis, which could be used to estimate the reaction plane in the Heavy Ion Collision.[3] In this analysis, we used STAR detector Event Plane Detector(EPD), incorporating with Time Projection Chamber to reconstruct Event Plane(EP), where EPD is an upgrade detector in the STAR Beam Energy Scan phase II.[4] There are 12 supersectors on EPD. And 31 tiles on each supersector are connected via optical fiber bundles. The tile performance would be affected by its own quality and the signal intensity it received. So the correction for each tile is necessary, which would be introduced as follow.

Recentering and shifting method are two methods which we applied to correct the raw event plane distribution. EPD is divided to four ring groups to facilitate EP reconstruction. There are 16 rings/rows on EPD. It is divided equally to four groups, each group have four rings. Fig. 2 show groups at EPD, named as A, B, C and D. The best EP should be the one in the forward eta

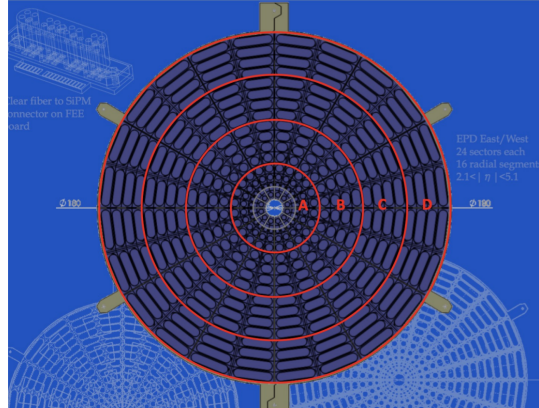


FIG. 2. The sketch of EPD groups.

range, where directed flow signal is greater than the one in middle eta range. [Analysis note](#) of one STAR published paper have approved it. We followed and chose EPD group A and B as target event plane in our analysis. In this way, we can get the largest resolution applied to our analysis according to equation 3

$$R_n \propto v_n \sqrt{M} \quad (3)$$

2.1.1. Recentering correction

The recentering calibration is applied to the flow vector(\vec{Q}), which could be decomposed into two components, as shown by equation 4, where w_i is EPD tile weight, using the calibrated value nMip(also known as ADC) based on the particle energy loss on each EPD tile, as shown by equation 5

$$\vec{Q} = \begin{pmatrix} Q_y \\ Q_x \end{pmatrix} = \begin{pmatrix} \sum_i w_i \sin(\phi_i) \\ \sum_i w_i \cos(\phi_i) \end{pmatrix} \quad (4)$$

$$w(\text{tile}) = \begin{cases} 0 & \text{if } nMIP < \text{threshold}(0.3) \\ \text{MAX} & \text{if } nMIP > \text{MAX}(2) \\ nMIP & \text{otherwise} \end{cases} \quad (5)$$

And the first order event plane angle could be obtained by equation 6, where ϕ_i is emitted particle angle with respect to the laboratory system, sums goes over all hits from one event.

$$\Psi_1 = \tan^{-1} \frac{\sum_i w_i \sin(\phi_i)}{\sum_i w_i \cos(\phi_i)} \quad (6)$$

The recentering method is applied to the flow vertex \vec{Q} , so it's event by event calibration, which is expressed by equation 7. The angle brackets denote averaging over all events in the same centrality and run ID.

$$\vec{Q}_{rc} = \begin{pmatrix} \vec{Q}_y - \langle \vec{Q}_y \rangle \\ \vec{Q}_x - \langle \vec{Q}_x \rangle \end{pmatrix} \quad (7)$$

2.1.2. Shifting correction

The shifting calibration is a mathematical method to correct the EP distribution after recentering calibration, which is based on Fourier transformation. In this analysis, a 20th order equation 8 was implemented to the event plane distribution after recentering calibration.

$$\Psi_{1, shift} = \sum_i^N \frac{2}{i} [-\langle \sin(i\Psi_{1,rc}) \rangle \cos(i\Psi_{1,rc}) + \langle \cos(i\Psi_{1,rc}) \rangle \sin(i\Psi_{1,rc})] \quad (8)$$

The angle brackets in the equation denote averaging over all events in the same centrality and run ID. And the final EP angle after recentering and shifting calibration could be obtained by equation 9

$$\Psi_1 = \Psi_{1,rc} + \Psi_{1,shift} \quad (9)$$

Fig. 3 show event plane distribution at 3, 3.2, 3.5 and 3.9 GeV based on all EPD rings, where the black line show the raw distribution without any calibration, the blue line represents the EP after recentering calibration, and red line denote the event plane angle distribution after recentering and shifting calibration, which is "flat".

2.1.3. Event plane resolution

After recentering and shifting calibration, the event plane is ready for the flow calculation. While the finite multiplicity in the experiment would limit the estimation of the reaction plane angle. [5] So the event plane resolution would be brought to correct the observed flow coefficients, which could be expressed as equation 10

$$R_n = \langle \cos[n(\Psi_n - \Psi_r)] \rangle \quad (10)$$

Where Ψ_r is reaction plane angle, Ψ_n is the event plane angle. The angle brackets denote averaging over many events.

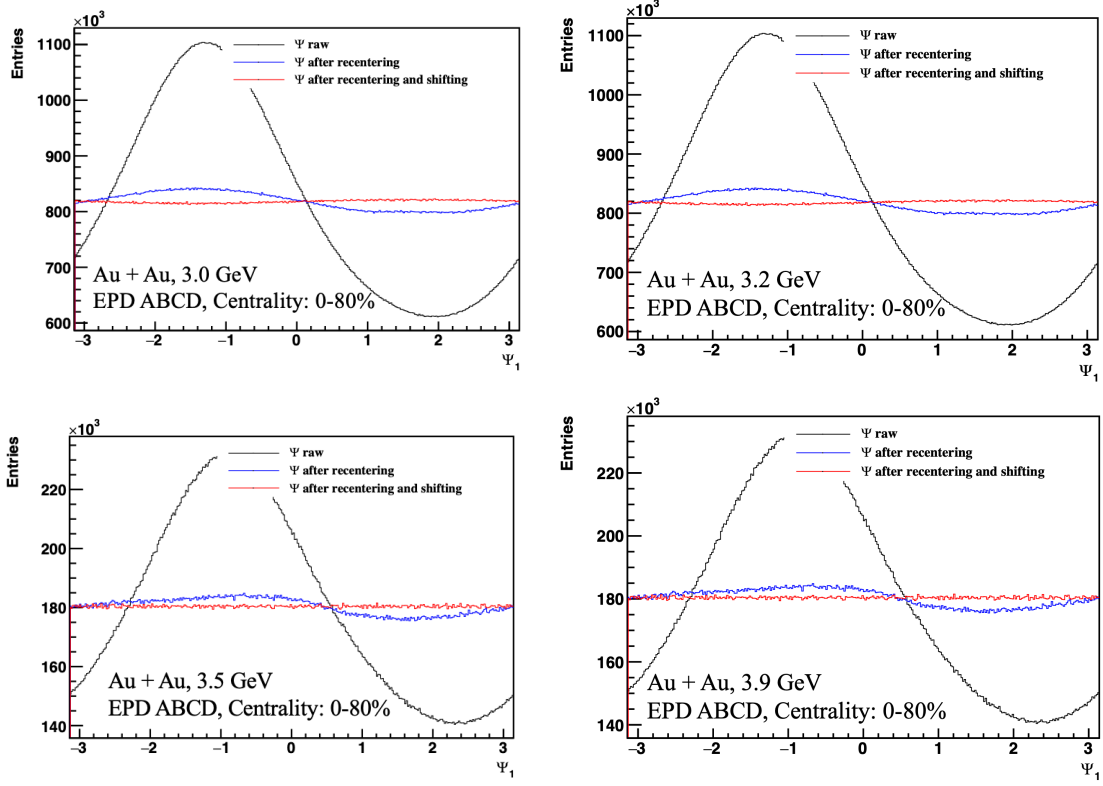


FIG. 3. The event plane distribution on EPD.

In the fixed target mode, one would not be able to get sub-events are equal, since the collision happens at the end of TPC. The resolution in different window are not equal, one need at least three windows to determine the event plane resolution in each of them. [6] It could be expressed as

$$\langle \cos(n(\Psi_m^a - \Psi_r)) \rangle = \sqrt{\frac{\langle \cos(n(\Psi_m^a - \Psi_m^b)) \rangle \langle \cos(n(\Psi_m^a - \Psi_m^c)) \rangle}{\langle \cos(n(\Psi_m^b - \Psi_m^c)) \rangle}} \quad (11)$$

Where Ψ_m^a is the target event plane angle, Ψ_m^b and Ψ_m^c are the reference event plane angle.

In this analysis, we focus on directed flow(v_1) measurement, they are both based on first order event plane. so we substitute $m = 1$ to the equation 11. According to the STAR published 3 GeV paper [7], One can get the largest resolution if chosen the forward eta window(EPD group A and B). We follow the method and take EPD group A and B as our target event plane. Other windows from EPD and TPC would be chosen as reference windows. They are divided as shown by Fig. 4 This figure is specific for 3.0 GeV. We note here eta could reach 2.4 for 3.2, 3.5 and 3.9 GeV data, since inner TPC was upgraded at these three energies. Two eta gaps were added in this analysis to reduce the non-flow effect. One eta gap is in the EPD group C which eta coverage is

$[-3.3, -3.0]$ (removed two EPD rings in C, here C' denotes group C after removing two rings), the other one is in the TPC which eta coverage is $[-1.1, -1.0]$ for 3GeV, while $[-1.15, -1.25]$ for 3.2, 3.5, and 3.9 GeV due to the wider eta coverage brought by iTPC.

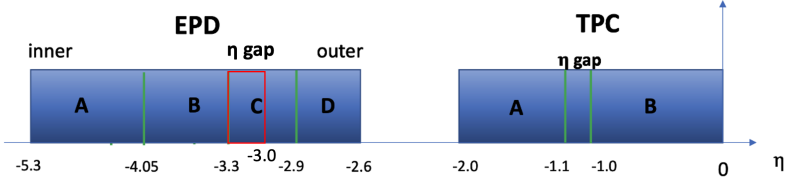


FIG. 4. The sketch of EPD and TPC groups.

The first order event plane resolution of EPD group AB at 3.0, 3.2, 3.5, and 3.9 GeV was shown by Fig. 5. EPD group AB was chosen as the target event plane, and another two reference event plane were needed according to three sub-event plane method. In this analysis, the maximum R_1 (EPD-AB vs. EPD-C' and TPC-B) was chosen as default resolution to measure directed flow, which could be expressed as:

$$v_n = \frac{v_n^{\text{obs}}}{R_n} \quad (12)$$

The other two set of resolution were used to estimate the systematic uncertainty brought by resolution.

2.2. Particle identification

2.2.1. π, K, p identification

Time Projection Chamber(TPC)[8] and Time of Flight(TOF)[9] were used to identify pion, kaon, and proton. The identification are based on particle ionization energy loss(dE/dx) in TPC and time of particle flight measured by TOF. The theoretic particle ionization energy loss could be described by Bichsel function, which are shown by dashed line in left panel of Fig. 6. The dE/dx value would be transformed to $n\sigma_{\text{particle}}$ to facilitate applying the PID cut. The $n\sigma_{\text{particle}}$ can be expressed as:

$$n\sigma_{\text{particle}} \propto \ln \left[\left\langle \frac{dE}{dX} \right\rangle_{\text{particle}} / \left\langle \frac{dE}{dX} \right\rangle_{\text{Bichsel}} \right] \quad (13)$$

In this analysis, we take the $n\sigma_{\text{particle}}$ shift into account which is due to detector issue and data calibration issue. For example, the $n\sigma_{\text{proton}}$ distribution in momentum windows are shown by

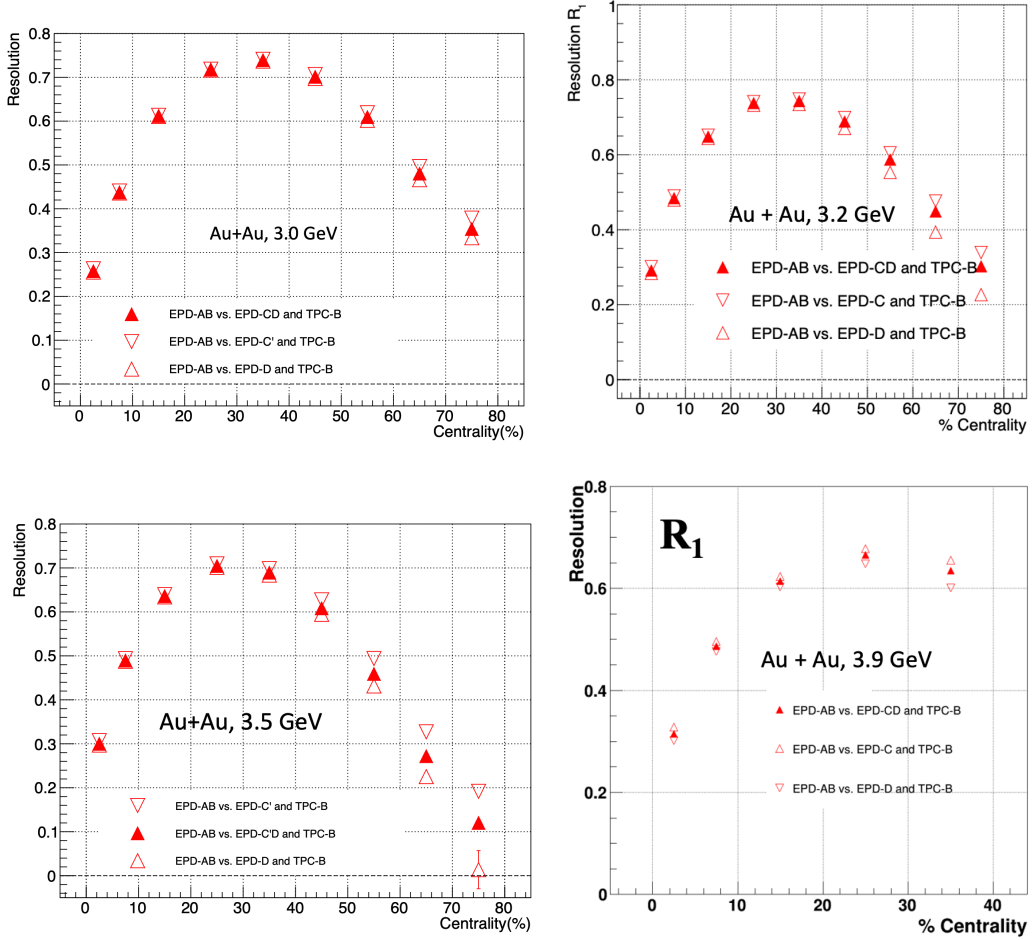


FIG. 5. The first order event plane resolution of EPD group AB at 3.0, 3.2, 3.5, and 3.9 GeV.

Fig. 7. The background and signal peak were fitted with Gaussian function, and proton purity could reach more than 95% up to momentum at 1.2 GeV/c. At higher momentum region($p > 1.2\text{GeV}/c$), the signal and background peak are merged, it's unable to assure proton purity greater than 95% with TPC alone. In that case, TOF was involved to help identify particle at high momentum.

The right panel of Fig. 6 show rigidity dependence of mass square(m^2) distribution measured by TOF, the m^2 could be calculated by the formula: $m^2 = p^2(1/\beta^2 - 1)$, where velocity $\beta = L/cT$. At high momentum, we used m^2 distribution instead to study the particle purity. The m^2 distribution is after $n\sigma_{particle}$ cut from TPC. For example, Fig. 8 show proton m^2 distribution in momentum windows after $|n\sigma_{proton} - shift| < 3$ cut. And Student-t function was applied to fit the signal peak and the background peak. By that way, proton identification could reach $p = 4.2 \text{ GeV}/c$, and the purity is greater than 95%. Purity of pion and kaon is greater than 95% and 90%, respectively. The detailed PID cuts are shown by the TABLE VI in the appendix for 3, 3.2, 3.5, and 3.9 GeV.

Daughters' track cuts	$nHitsFit > 15$	$ n\sigma_{\pi,p} - shift < 3$, $\pi^+ : -0.06 < m^2 < 0.1$	$0.04 < Error(dE/dx) < 0.12$	$nHitsdEdx > 5$
Topological cuts	$\chi^2_{prim,\pi} < 10$	$\chi^2_{prim,p} < 10$		

TABLE III. Daughters' track cuts and topological cuts applied for K_S^0, Λ in KF particle

The acceptance of π, K, p at 3.5 GeV are shown by Fig. 9, the black box show the measured arear, where the rapidity cut is $-1 < y_{CM} < 0$, and p_T cut are $0.2 < p_T < 1.6, 0.4 < p_T < 2.0$ for π/K , proton, respectively. For other energies, 3(Fig. 34), 3.2, and 3.9 GeV, the acceptance plots could be found in the appendix.

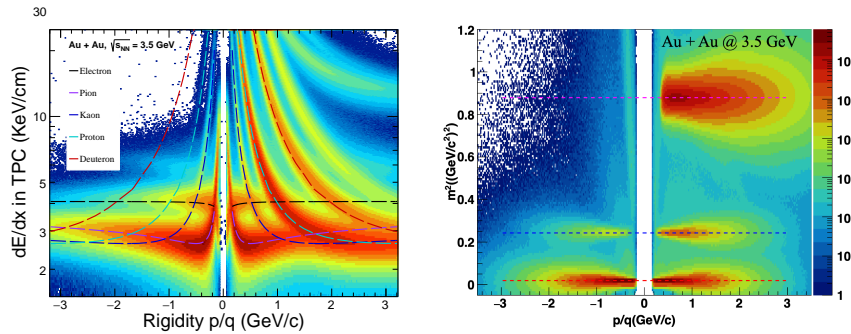


FIG. 6. Left: rigidity dependence of particle ionization energy loss in TPC, Right: rigidity dependence of particle mass square distribution measured by TOF in Au + Au collisions at $\sqrt{s_{NN}} = 3.5$ GeV.

2.2.2. K_S^0, Λ identification

For the weak decay particles K_S^0 and Λ , they are reconstructed by Kalman Filter(KF) particle package[10], where the covariance matrix of reconstructed tracks are considered to construct a set of topological variable. The track and topological cuts for daughters are listed in the TABLE. III. Note that only π^+ was required to have m^2 cut to avoid contamination from proton.

The acceptance of K_S^0 and Λ are shown by Fig. 10. The black box show the kinematic region chosen in this analysis, where the rapidity cut is $-1 < y_{CM} < 0$, and p_T cut are $0.2 < p_T < 1.6, 0.4 < p_T < 2.0$ for K_S^0 and Λ , respectively. The acceptance plots could be found in the appendix for other energies(3GeV(Fig. 35), 3.2 GeV, 3.9 GeV).

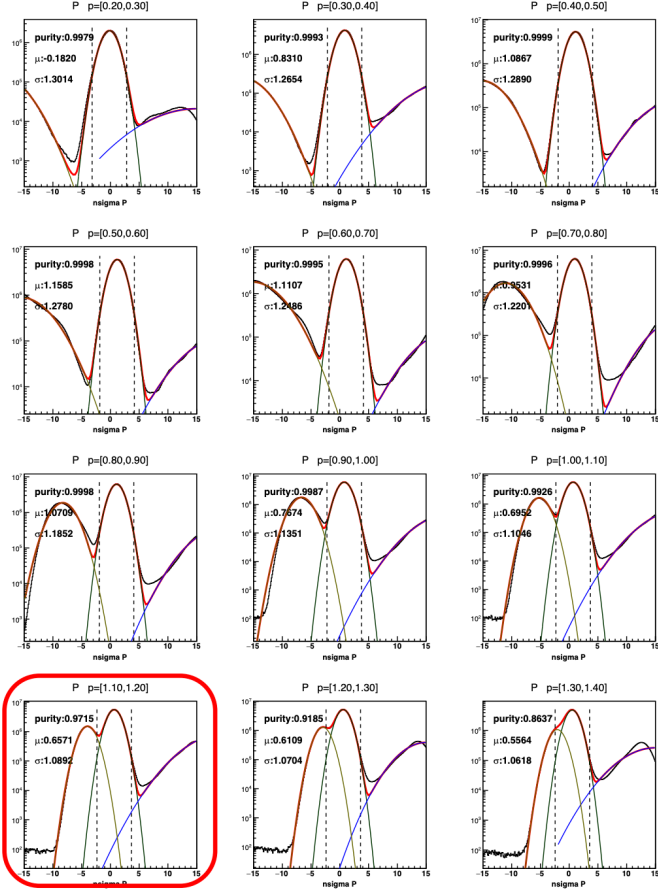


FIG. 7. $n\sigma_{proton}$ distribution in momentum windows from TPC at $\sqrt{s_{NN}} = 3.5$ GeV.

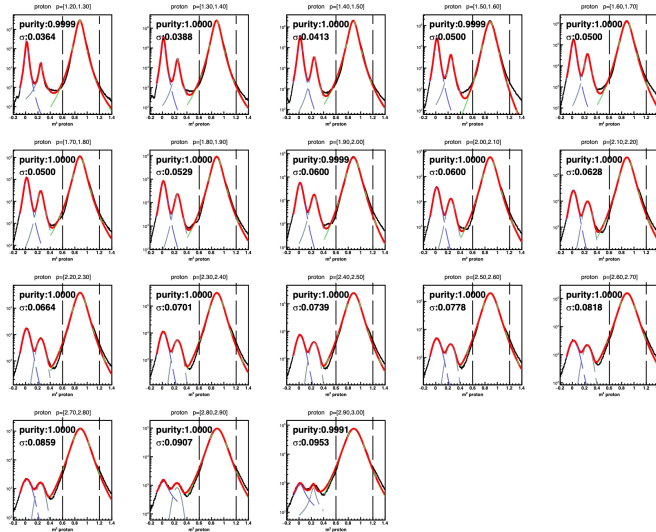


FIG. 8. m^2 distribution in momentum windows from TOF at $\sqrt{s_{NN}} = 3.5$ GeV.

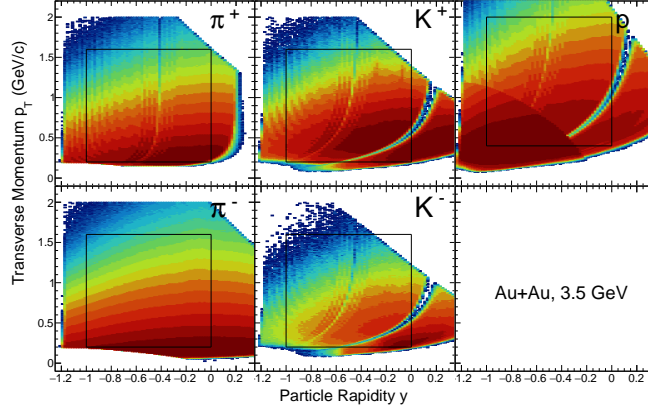


FIG. 9. π, K, p density distribution as function of rapidity and transverse momentum at $\sqrt{s_{NN}} = 3.5$ GeV.

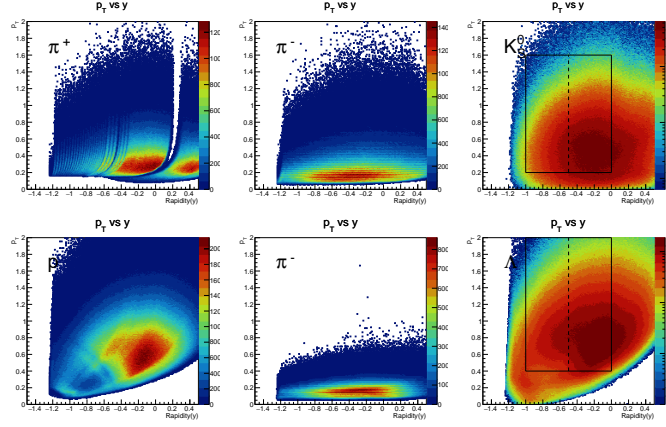


FIG. 10. K_S^0 and Λ (and their daughters) density distribution as function of rapidity and transverse momentum at $\sqrt{s_{NN}} = 3.5$ GeV.

2.3. Efficiency correction

The efficiency correction would help to restore the particle which was not tracked by the detector. In this analysis, TPC tracking efficiency and TOF matching efficiency are taken into account for π, K , and p . For the weak decay particles(K_S^0 and Λ) which are reconstructed by KF particle package, the reconstruction efficiency was applied instead.

The GEANT model[11] was used to simulate particle going through the detector based on Monte Carlo method, which could estimate the particle number loss due to the detector acceptance and the efficiency of reconstructing particle track. For K_S^0 and Λ , the GEANT model can also estimate the particle reconstruction efficiency.

The TPC tracking efficiency as function of rapidity and transverse momentum could be obtained by the formula 14

$$\epsilon_{TPC}(p_T, y) = \frac{\text{Number of Real Tracks}}{\text{Number of MC Tracks}} \quad (14)$$

The embedding data used in this analysis could be found at the RCF:

/star/u/xgn1992/Strangeness/Phi/3p85GeV_fixTarget/SL19e/Simulation/Embedding
for 3 GeV, /star/data105/embedding/production_4p59_fixedTarget_2019 for 3.2 GeV.

The TPC tracking efficiency for π, K, p are shown by Fig. 11 at 3.2 GeV. The black box show the measured rapidity and transverse momentum interval, where the rapidity cut is $-1 < y_{CM} < 0$, and p_T cut are $0.2 < p_T < 1.6, 0.4 < p_T < 2.0$ for π/K and p , respectively. For other energies, the TPC tracking efficiency can be found in the appendix.(3GeV(Fig 36), 3.5GeV, 3.9GeV)

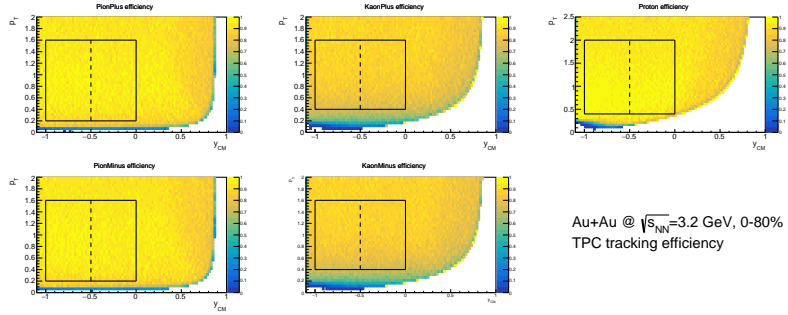


FIG. 11. TPC tracking efficiency of π, K, p as function of rapidity y and transverse momentum p_T at $\sqrt{s_{NN}} = 3.2$ GeV.

The TOF can improve the particle identification capability at high momentum region, which is necessary for kaon identification, discussed in the PID section. While some particles which have tracks in TPC can not travel into TOF, and are not recorded by TOF. The TOF matching efficiency could compensate to the un-recorded part, which can be expressed by the formula 15. Note that TPC tracks are required within $|n\sigma_{particle} - shift| < 3$, and TOF tracks just are required the TOF match flag is greater than zero.

$$\epsilon_{TOF}(p_T, y) = \frac{\text{Number of TOF Tracks}}{\text{Number of TPC Tracks}} \quad (15)$$

The TOF matching efficiency for π, K, p are shown by Fig. 12 at 3.2 GeV. The black box show the measured rapidity and transverse momentum interval, where the rapidity cut is $-1 < y_{CM} < 0$, and p_T cut are $0.2 < p_T < 1.6, 0.4 < p_T < 2.0$ for π/K and p , respectively. For other energies, the TOF matching efficiency can be found in the appendix.(3GeV(Fig 37), 3.5GeV, 3.9GeV)

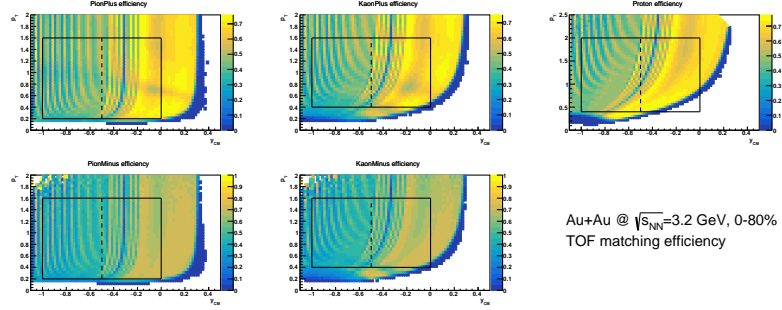


FIG. 12. TOF matching efficiency of π, K, p as function of rapidity y and transverse momentum p_T at $\sqrt{s_{NN}} = 3.2$ GeV.

The reconstruction efficiency for K_S^0 and Λ can be obtained by the formula 16, which are shown by Fig. 13 at 3.2 GeV. The black box show the measured rapidity and transverse momentum interval, where the rapidity cut is $-1 < y_{CM} < 0$, and p_T cut are $0.2 < p_T < 1.6, 0.4 < p_T < 2.0$ for K_S^0 and Λ , respectively. Note that the track and topological cuts applied are identical with identification cuts which is shown by the TABLE. III. For other energies, the TPC tracking efficiency can be found in the appendix.(3GeV(Fig 38), 3.5GeV, 3.9GeV)

$$\epsilon(p_T, y) = \frac{\text{Number of Reconstructed Tracks}}{\text{Number of MC Tracks}} \quad (16)$$

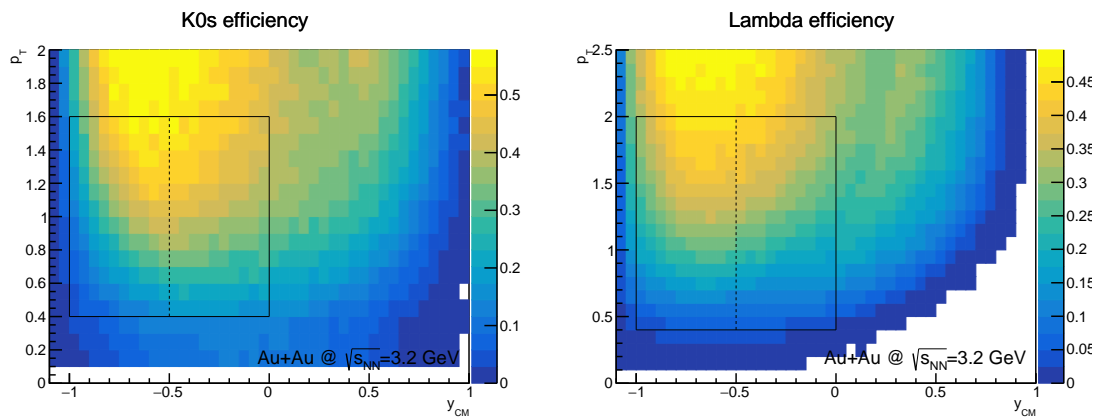


FIG. 13. Reconstruction efficiency of K_S^0 (Left), Λ (Right) as function of rapidity y and transverse momentum p_T at $\sqrt{s_{NN}} = 3.2$ GeV.

3. RESULTS

In this section, v_1 of π , K , p , K_S^0 and Λ are presented as function of rapidity and transverse momentum at $\sqrt{s_{NN}} = 3.0, 3.2, 3.5, 3.9$ GeV. π , K , p v_1 were extracted based on event plane method, K_S^0 and Λ v_1 were extracted by invariant mass method. And the systematic uncertainty study was involved at the end of section.

3.1. Directed flow of π , K , p

3.1.1. Rapidity dependence of v_1

Fig. 14 shows rapidity dependence of pions, kaons, and proton v_1 within 0-10%, 10-40%, 40-60% centrality at $\sqrt{s_{NN}} = 3.5$ GeV, where the p_T cut are $0.2 < p_T < 1.6$ GeV/c , $0.4 < p_T < 1.6$ GeV/c , $0.4 < p_T < 2.0$ GeV/c for pions, kaons, and proton, respectively.

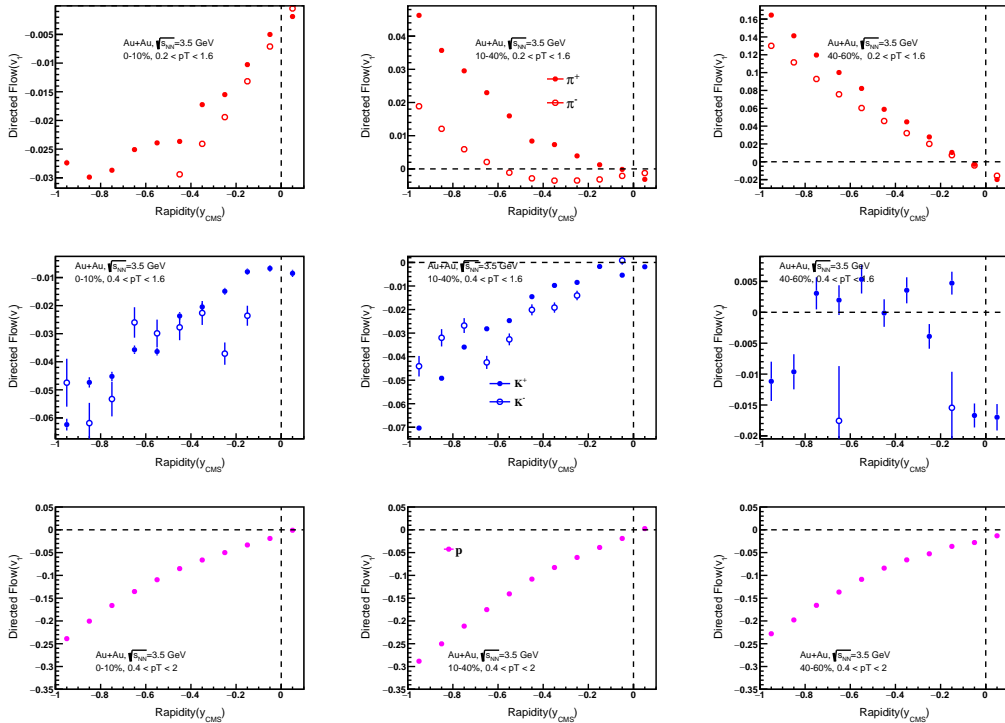


FIG. 14. v_1 of pions, kaons, and proton as function of rapidity at $\sqrt{s_{NN}} = 3.5$ GeV.

3.1.2. Transverse momentum dependence of $v_1(y)$

Fig. 15 shows rapidity dependence of pion v_1 within p_T windows in 10-40% centrality at $\sqrt{s_{NN}} = 3.5$ GeV. And results in other centralities could be found in the appendix(0-10%(Fig. 40), 40-60%(Fig. 39)) Note that the solid and dashed line in the plots are cubic function: $v_1(y) = a*y + b*y^3$. The coefficient of the linear term "a" is so called v_1 slope in the mid-rapidity($dv_1/dy|_{y=0}$).

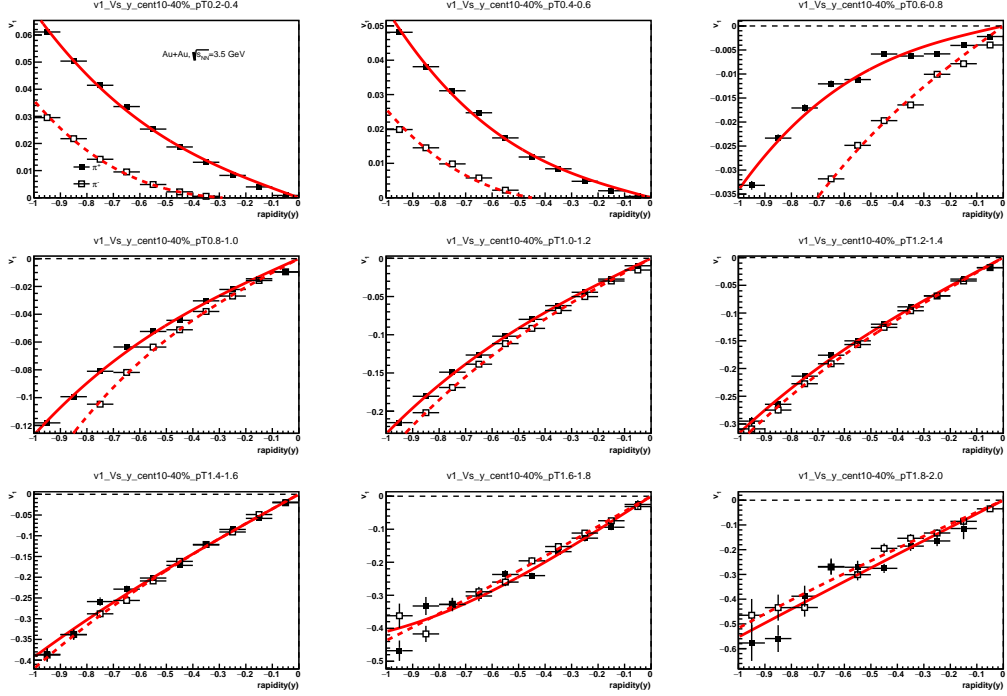


FIG. 15. v_1 of pions as function of rapidity within p_T windows in 10-40% centrality at $\sqrt{s_{NN}} = 3.5$ GeV.

The p_T dependence of v_1 slope is summarized in the Fig. 16 for $\sqrt{s_{NN}} = 3.5$ GeV. Pion v_1 strength in the mid-rapidity show strong p_T and centrality dependence, in the very-central collisions(0-10%), there is no anti-flow(negative v_1 slope) at low p_T for pions, while the slopes at low p_T turn to negative in the mid-central and peripheral collisions. In particular, the negative slopes are largest in magnitude in the peripheral collisions. The centrality dependence of v_1 slope indicates that the pion anti-flow at low p_T is due to shadowing effect from spectator.

Fig. 17 and Fig. 18 show p_T dependence of v_1 slope for kaons and proton, respectively. The fitting plots could be found in the appendix.(Kaons:0-10%(Fig. 43), 10-40%(Fig. 42), 40-60%(Fig. 41). proton: 0-10%(Fig. 46), 10-40%(Fig. 45), 40-60%(Fig. 44)). Kaons show anti-flow at low p_T in the three centralities, while proton baryon didn't show anti-flow at low pT(positive slope in the three centralities). The particle species dependence implies that the shadowing ef-

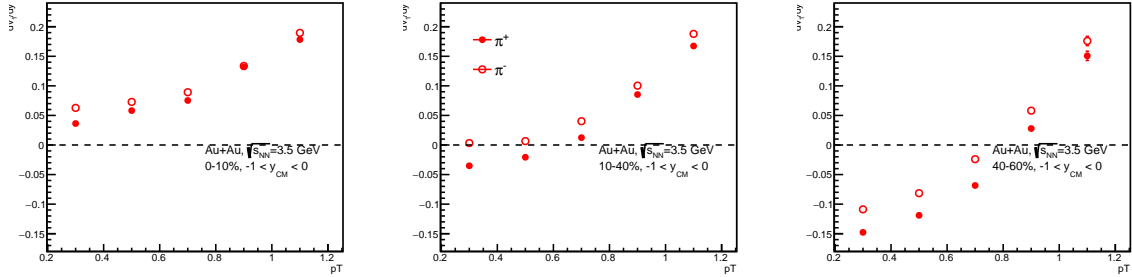


FIG. 16. $dv_1/dy|_{y=0}$ of pions as function of p_T at $\sqrt{s_{NN}} = 3.5$ GeV.

fect impact on the lighter meson and result in anti-flow at low p_T . The heavy baryon may go through the participant matter and remaining spectator without suffering strong shadowing effect as mesons.

For other energies, Fig. 47, Fig. 48, and Fig. 49 in the appendix show p_T dependence of v_1 slope for pions, kaons, and proton at $\sqrt{s_{NN}} = 3.0$ GeV, respectively.

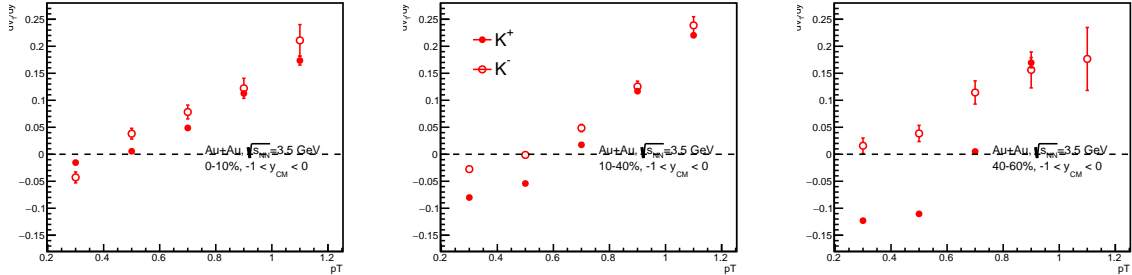


FIG. 17. $dv_1/dy|_{y=0}$ of kaons as function of p_T at $\sqrt{s_{NN}} = 3.5$ GeV.

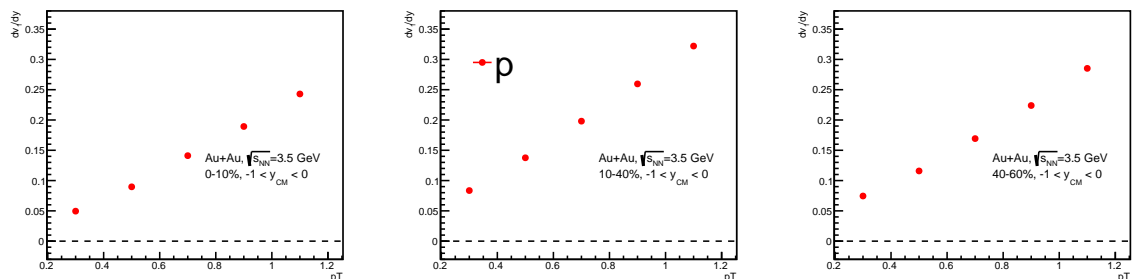


FIG. 18. $dv_1/dy|_{y=0}$ of proton as function of p_T at $\sqrt{s_{NN}} = 3.5$ GeV.

Cuts	Default	var1	var2
DCA(<)	3	1	2
nHitsFit(>)	15	20	25
$n\sigma_{particle}(<)$	3	2	2.5
m_π^2	[-0.1,0.15]	[-0.05,0.1]	
m_K^2	[0.16,0.36]	[0.18,0.32]	
m_p^2	[0.6, 1.2]	[0.7, 1.1]	
R_{11}	EPD-C'	EPD-D	

TABLE IV. Systematic uncertainty sources for π , K, p. Note that EPD-C' is EPD-AB vs. EPD-C' and TPC-B, and EPD-D is EPD-AB vs. EPD-D and TPC-B, which are shown in the Fig. 5

3.1.3. Systematic uncertainty

The systematic uncertainty study could take random uncertainties into account [12], which are brought by detector effect, particle identification, and flow measurement method, etc. In this analysis, we take track quality cuts (DCA and nHitsFit), PID cuts ($n\sigma_{particle}$ and m^2), and resolution as systematic uncertainty sources. TABLE IV show the systematic uncertainty sources chosen for directed measurement of π , K, p. We assume that these sources are uncorrelated. According to Barlow Test [12], the differences between the default source and the variation are required to be smaller than the one of their statistical uncertainties, otherwise it would not be taken as systematic uncertainty since the statistical fluctuation dominants. At last, the maximum deviation from the default value was chosen as the systematic uncertainty. The total systematic uncertainties could be obtained by the equation 17.

$$\text{sys.}Unc_{\text{total}} = \sqrt{\left(y_{DCA} - y_{def}\right)^2 + \left(y_{nHitsFit} - y_{def}\right)^2 + \left(y_{n\sigma} - y_{def}\right)^2 + \left(y_{m^2} - y_{def}\right)^2 + \left(y_{Res} - y_{def}\right)^2} \quad (17)$$

Fig. 19 illustrates the rapidity dependence of v_1 for pions from various systematic sources at $\sqrt{s_{NN}} = 3.5$ GeV. v_1 of pions in the mid-central collisions are shown by Fig. 20, where the bands stand for the systematic errors. And Fig. 21 show $v_1(y)$ of π^+ within narrow p_T windows, the v_1 slopes extracted in the mid-rapidity are summarized with Fig. 22. At last, Fig. 23 illustrates p_T dependence of v_1 slope for pions, where π^+ shows anti-flow at low p_T , π^- shows positive slopes.

It might be explained by Columb effect. For other particles(kaons and proton) and other energies, the similary plots could be found in the appendix.

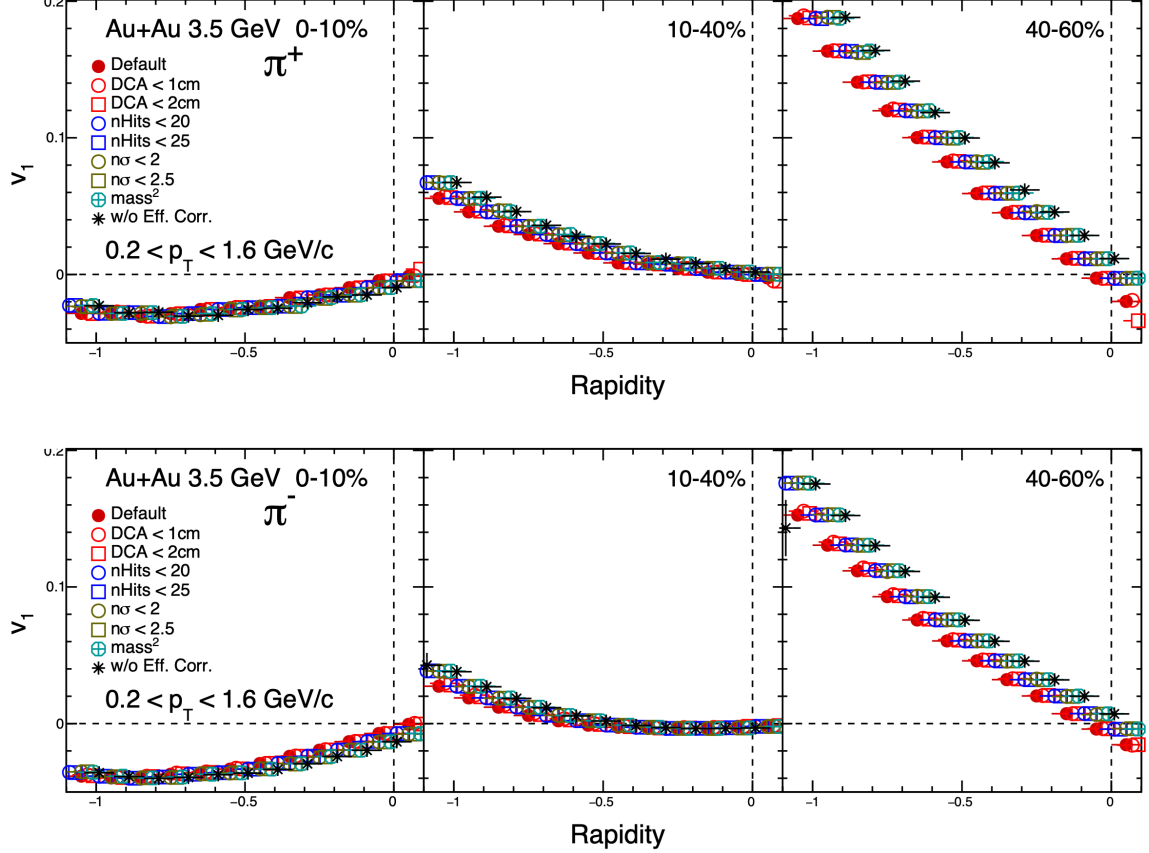


FIG. 19. v_1 of pions as function of rapidity from systematic sources at $\sqrt{s_{NN}} = 3.5$ GeV.

3.2. Directed flow of K_S^0, Λ

Invariant mass method is applied to extract v_1 of K_S^0 and Λ . The ideal of this method is to seperate v_1 of signal from backgroud, where the v_1 of signal and backgroud could be expressed as equation 18. Note that "Sig" denotes the signal yield, "Bg" denotes the backgroud yield, and v_1 of backgroud is taken as the second order polynomial function, v_1^{Sig+Bg} is calculated by $v_1^{Sig+Bg} = <\cos(\phi - \Psi_{EP})>/R_1$. Then, v_1^{Sig} in various rapidity bins could be extracted by fitting the invariant mass distribution, which are shown by Fig. 24

$$v_1^{Sig+Bg}(m_{inv}) = \frac{Sig}{Sig + Bg} v_1^{Sig} + \frac{Bg}{Sig + Bg} v_1^{Bg} \quad (18)$$

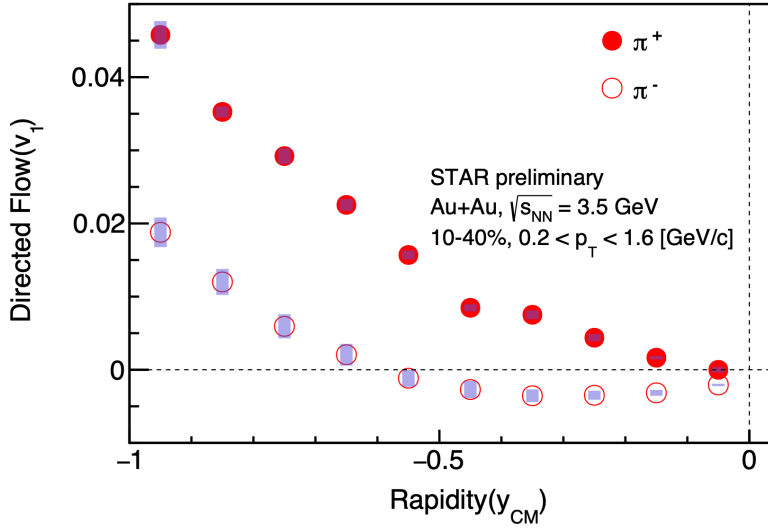


FIG. 20. v_1 of pions as function of rapidity at $\sqrt{s_{NN}} = 3.5$ GeV.

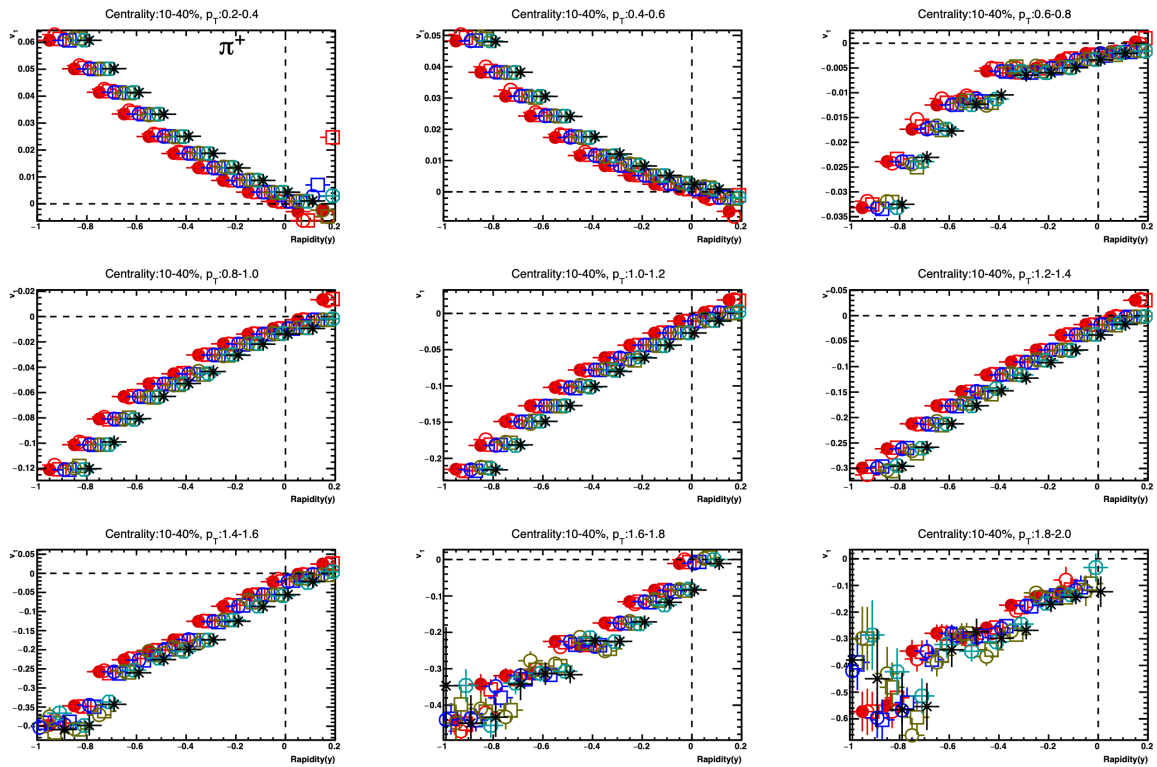


FIG. 21. v_1 of π^+ as function of rapidity within p_T windows at $\sqrt{s_{NN}} = 3.5$ GeV.

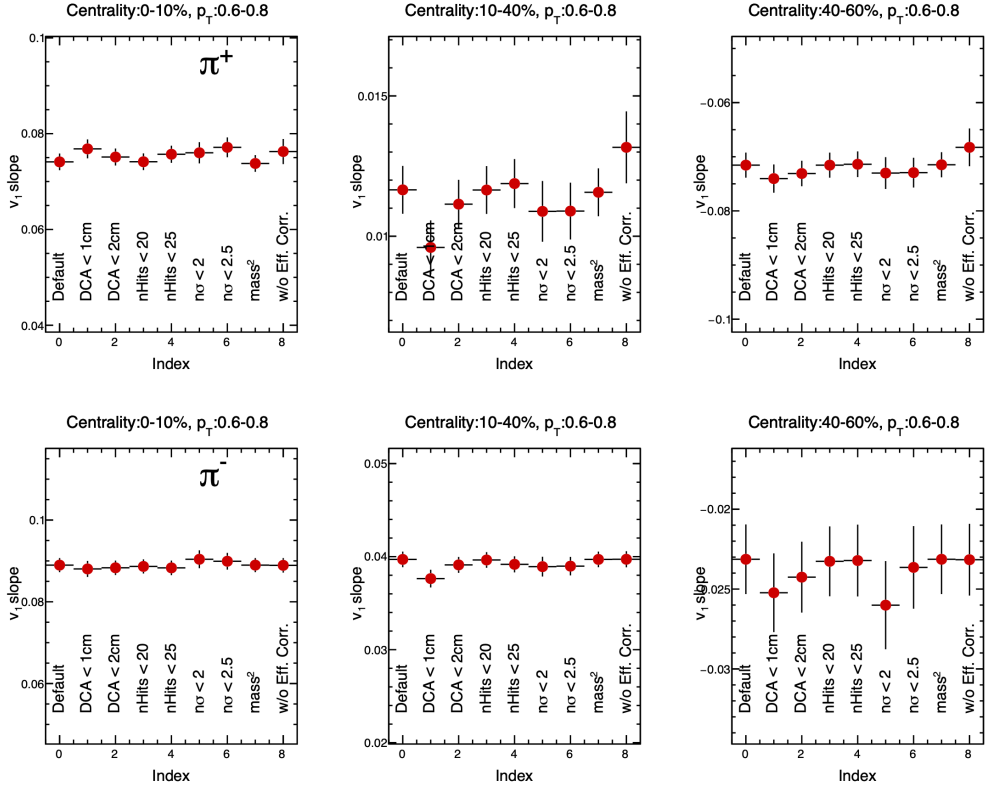


FIG. 22. v_1 slope of pions as function of systematic sources at $\sqrt{s_{NN}} = 3.5$ GeV.

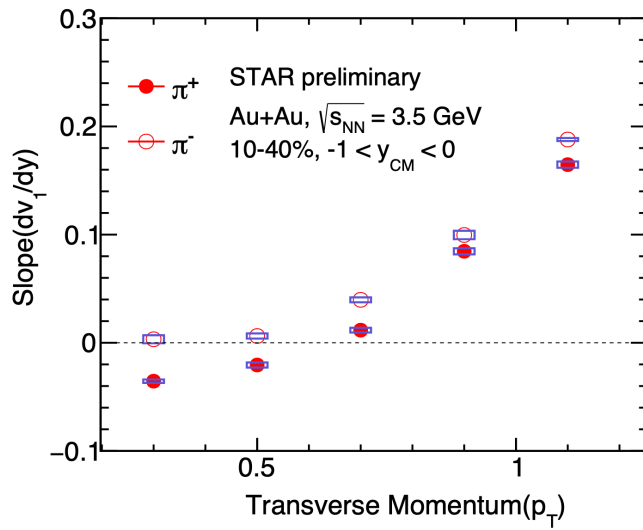


FIG. 23. v_1 slope of pions as function of transverse momentum at $\sqrt{s_{NN}} = 3.5$ GeV.

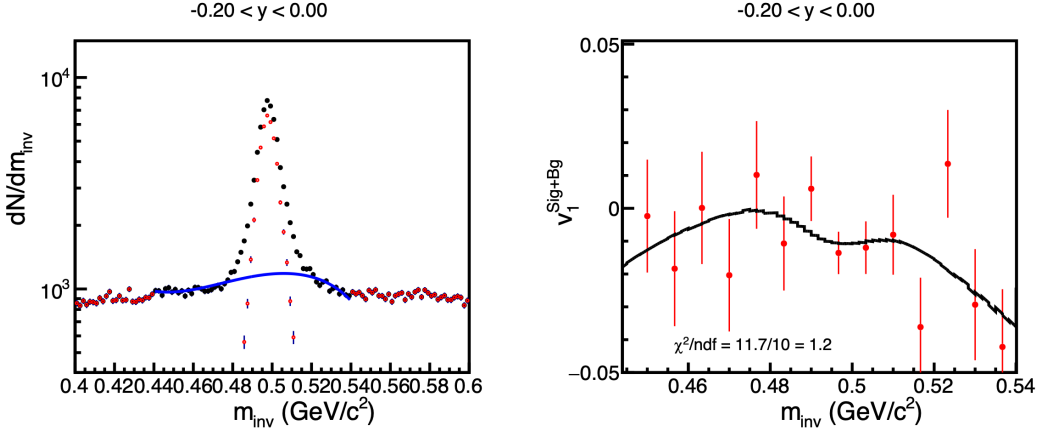


FIG. 24. Invariant mass distribution of K_S^0 in 10-40% centrality at $\sqrt{s_{NN}} = 3.5$ GeV.

3.2.1. Rapidity dependence of v_1

Fig. 25 shows rapidity dependence of K_S^0 and Λ v_1 within 10-40% centrality at $\sqrt{s_{NN}} = 3.5$ GeV, where the p_T cut are $0.4 < p_T < 1.6$ GeV/ c , $0.4 < p_T < 2.0$ GeV/ c for K_S^0 and Λ , respectively.

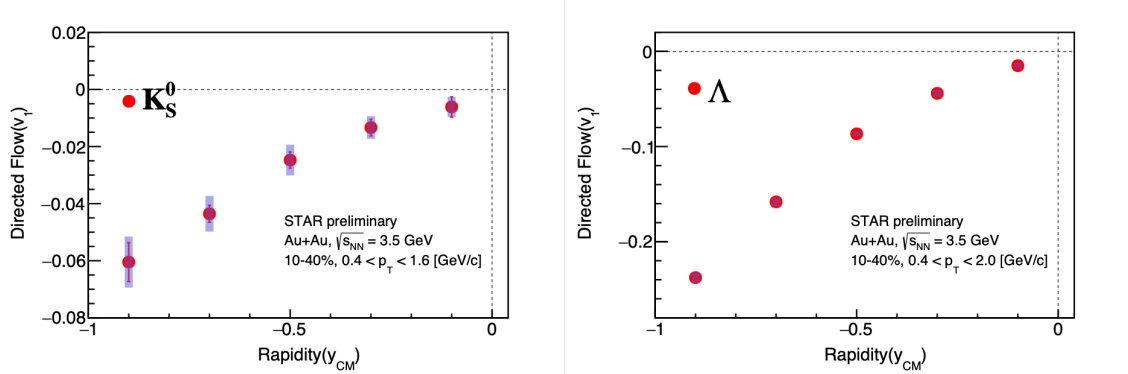


FIG. 25. v_1 of K_S^0 and Λ as function of rapidity at $\sqrt{s_{NN}} = 3.5$ GeV.

3.2.2. Transverse momentum dependence of $v_1(y)$

Fig. 26 shows rapidity dependence of K_S^0 and Λ v_1 within p_T windows in 10-40% centrality at $\sqrt{s_{NN}} = 3.5$ GeV. Note that the solid and dashed line in the plots are cubic function: $v_1(y) = a * y + b * y^3$. The coefficient of the linear term "a" is so called v_1 slope in the mid-rapidity($dv_1/dy|_{y=0}$).

Fig. 27 show p_T dependence of v_1 slope for K_S^0 and Λ , respectively. K_S^0 show negative v_1 slopes at low p_T ($p_T < 0.6$ GeV/ c), which behaviors like charged kaons, while there is no anti-flow for Λ .

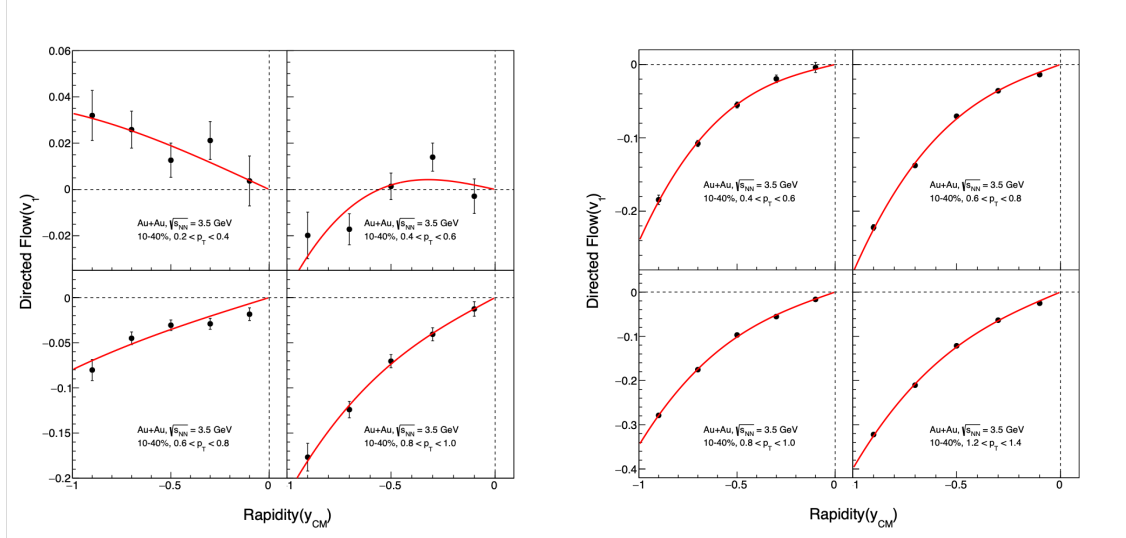


FIG. 26. v_1 of K_S^0 (left) and Λ (right) as function of rapidity within p_T windows in 10-40% centrality at $\sqrt{s_{NN}} = 3.5$ GeV.

at low p_T .

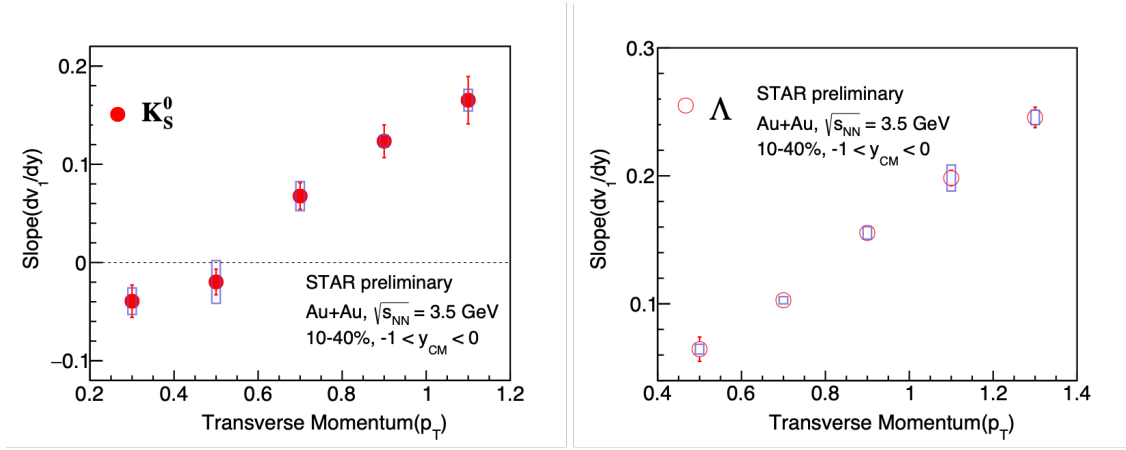


FIG. 27. v_1 slope of K_S^0 (left) and Λ (right) as function of p_T in 10-40% centrality at $\sqrt{s_{NN}} = 3.5$ GeV.

3.2.3. Systematic uncertainty

For systematic uncertainty estimate of K_S^0 and Λ v_1 , which are reconstructed by KF particle package, we take track quality cut (nHitsFit), PID cuts ($n\sigma_{particle}$ and χ^2_{prim} of daughters), and resolution as systematic uncertainty sources. TABLE V show the systematic uncertainty sources chosen for directed measurement of π , K , p . We assume that these sources are uncorrelated.

Cuts	Default	var1	var2
nHitsFit(>)	15	20	25
χ^2_{prim}	10	5	15
$n\sigma_{particle}$	3	2	2.5
R_{11}	EPD-C'	EPD-D	

TABLE V. Systematic uncertainty sources for K_S^0 and Λ , Note that EPD-C' is EPD-AB vs. EPD-C' and TPC-B, and EPD-D is EPD-AB vs. EPD-D and TPC-B, which are shown in the Fig. 5

According to Barlow Test [12], the differences between the default source and the variation are required to be smaller than the one of their statistical uncertainties, otherwise it would not be taken as systematic uncertainty since the statistical fluctuation dominants. At last, the maximum deviation from the default value was chosen as the systematic uncertainty. The total systematic uncertainties could be obtained by adding uncertainties brought from each sources in quadrature, which could be expressed as the equation 19.

$$sys.Unc_{total} = \sqrt{\left(y_{nHitsFit} - y_{def}\right)^2 + \left(y_{\chi^2_{prim}} - y_{def}\right)^2 + \left(y_{n\sigma} - y_{def}\right)^2 + \left(y_{Res} - y_{def}\right)^2} \quad (19)$$

Fig. 28 and Fig. 29 illustrate the rapidity dependence of v_1 from various systematic sources at $\sqrt{s_{NN}} = 3.5$ GeV for K_S^0 and Λ , respectively. Fig. 30 and Fig. 31 show $v_1(y)$ within narrow p_T windows of K_S^0 and Λ , respectively. The v_1 slopes extracted in the mid-rapidity are summarized with Fig. 32 and Fig. 33.

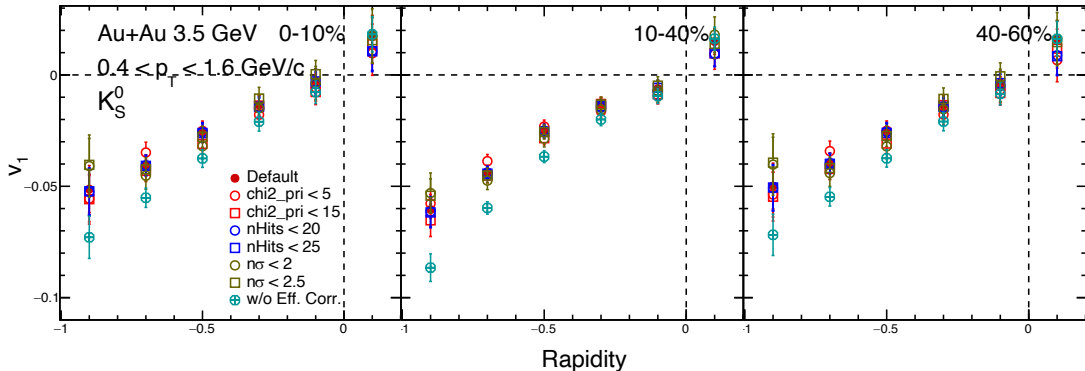


FIG. 28. v_1 of K_S^0 as function of rapidity from systematic sources at $\sqrt{s_{NN}} = 3.5$ GeV.

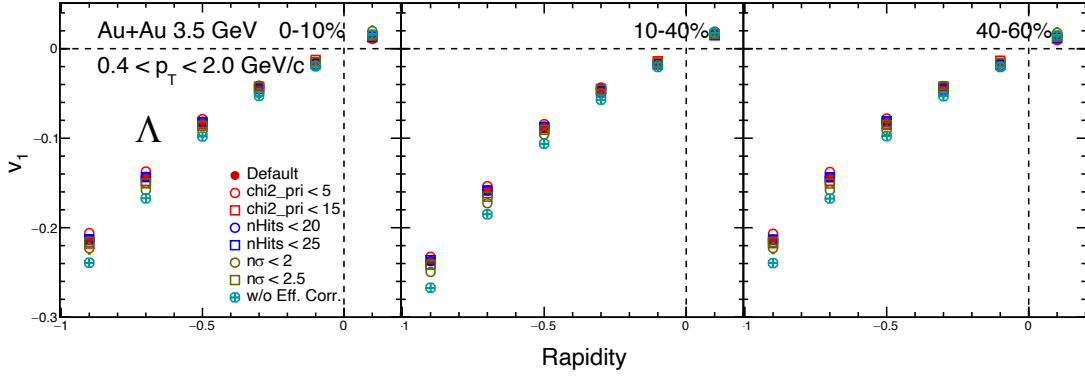


FIG. 29. v_1 of Λ as function of rapidity from systematic sources at $\sqrt{s_{NN}} = 3.5$ GeV.

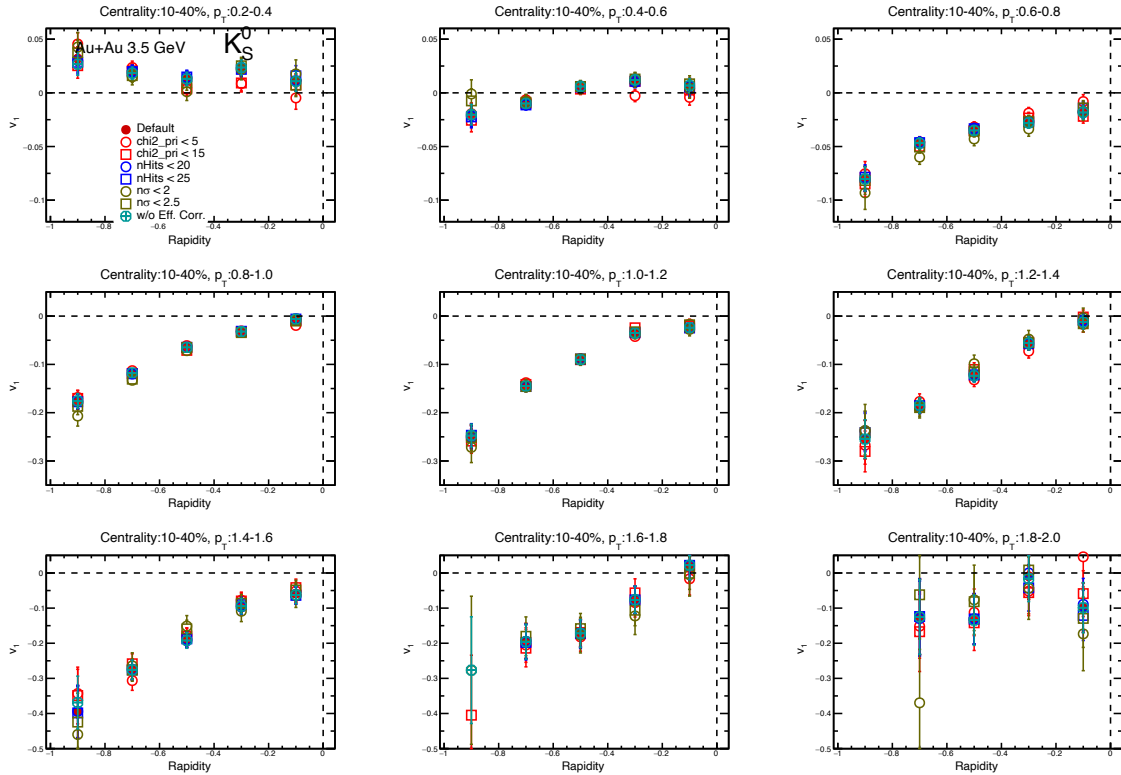


FIG. 30. v_1 of K_S^0 as function of rapidity within p_T windows at $\sqrt{s_{NN}} = 3.5$ GeV.

4. SUMMARY

We present directed flow measurement for π^\pm, K^\pm, p and K_S^0, Λ in Au + Au collisions at $\sqrt{s_{NN}} = 3.0, 3.2, 3.5$, and 3.9 GeV. The p_T dependence of v_1 slope in the mid-rapidity shows that there is anti-flow at low p_T ($p_T < 0.6$ GeV/c) for π^+ and kaons (K^\pm, K_S^0) in the mid-central 10 - 40%

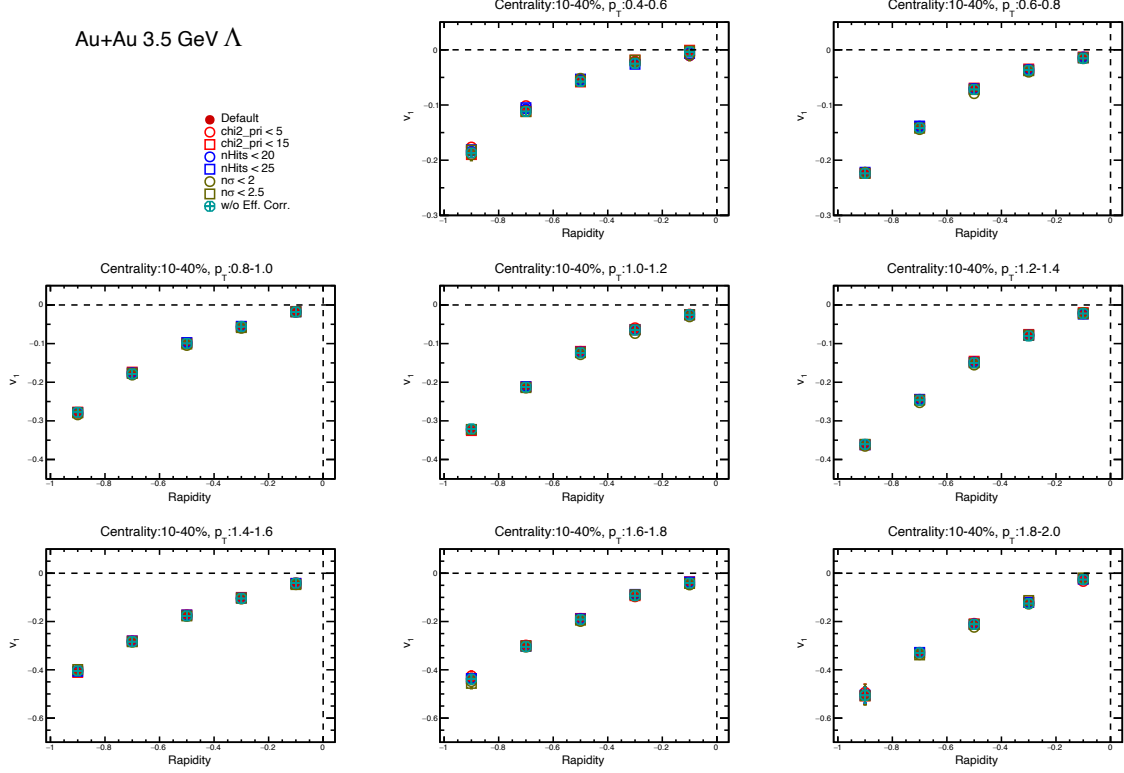


FIG. 31. v_1 of Λ as function of rapidity within p_T windows at $\sqrt{s_{NN}} = 3.5$ GeV.

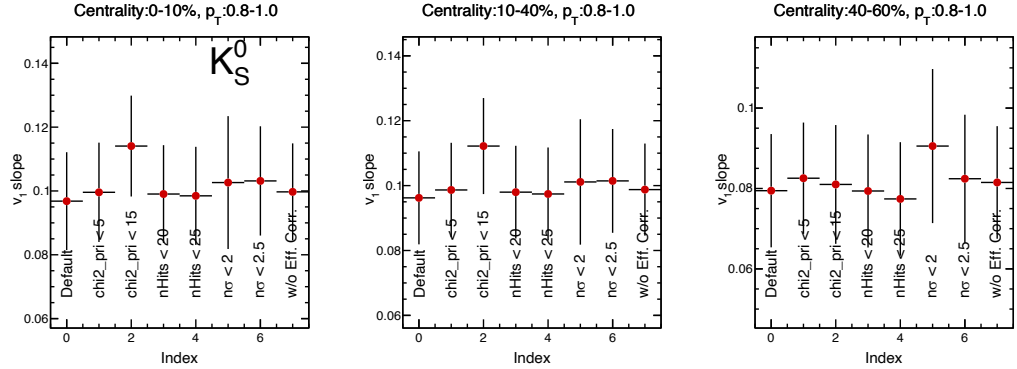


FIG. 32. v_1 slope of K_S^0 as function of systematic sources at $\sqrt{s_{NN}} = 3.5$ GeV.

collisions. By contrast, the baryons (proton and lambda) don't show anti-flow low p_T . Moreover, the centrality dependence of dv_1/dy shows that more negative v_1 slope could be observed in the more peripheral collisions. It indicates that the anti-flow might be related with spectator shadowing effect. At last, the JAM model calculation can reproduce anti-flow at low p_T without incorporating kaon potential. With the data measurement and model calculation, we conclude that the spectator

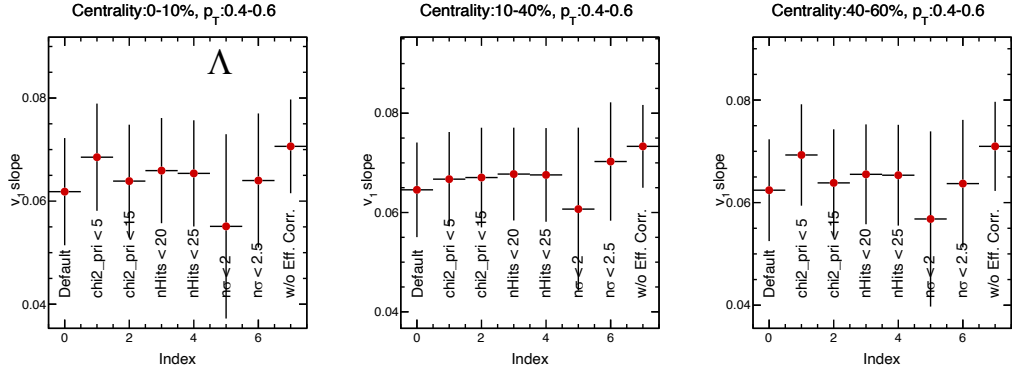


FIG. 33. v_1 slope of Λ as function of systematic sources at $\sqrt{s_{NN}} = 3.5$ GeV.

shadowing effect can lead to anti-flow of kaons, no need of the earlier claimed kaon potential.

	π^+	π^-	K^+	K^-	p
3.0 GeV	$ n\sigma_\pi < 3,$ $-0.1 < m^2 < 0.15$	$ n\sigma_\pi < 3,$ $-0.1 < m^2 < 0.15$	$ n\sigma_K < 3,$ $0.16 < m^2 < 0.36$	$ n\sigma_K < 3,$ $0.16 < m^2 < 0.36$	$p < 2GeV/c,$ $ n\sigma_p - shift < 2;$ $p > 2GeV/c,$ $ n\sigma_p - shift < 2,$ $0.6 < m^2 < 1.2$
3.2 GeV	$0.2 < p < 0.7GeV/c,$ $ n\sigma_\pi - shift < 3;$ $0.7 < p < 3.0GeV/c,$ $ n\sigma_\pi - shift < 3,$ $-0.1 < m^2 < 0.15$	$0.2 < p < 3.7GeV/c,$ $ n\sigma_\pi - shift < 3$	$0.2 < p < 2.1GeV/c,$ $ n\sigma_K - shift < 3,$ $0.16 < m^2 < 0.36;$ $2.1 < p < 2.6GeV/c,$ $ n\sigma_K - shift < 3,$ $0.2 < m^2 < 0.33$	$0.2 < p < 1.3GeV/c,$ $ n\sigma_K - shift < 3,$ $0.16 < m^2 < 0.36;$ $1.3 < p < 2.1GeV/c,$ $ n\sigma_K - shift < 3,$ $0.19 < m^2 < 0.36$	$0.2 < p < 1.3GeV/c,$ $ n\sigma_p - shift < 3;$ $1.3 < p < 4.5GeV/c,$ $ n\sigma_p - shift < 3,$ $0.6 < m^2 < 1.2$
3.5 GeV	$0.2 < p < 0.7GeV/c,$ $ n\sigma_\pi - shift < 3;$ $0.7 < p < 3.0GeV/c,$ $ n\sigma_\pi - shift < 3,$ $-0.1 < m^2 < 0.15$	$0.2 < p < 3.7GeV/c,$ $ n\sigma_\pi - shift < 3$	$0.2 < p < 2.3GeV/c,$ $ n\sigma_K - shift < 3,$ $0.16 < m^2 < 0.36;$ $2.3 < p < 2.7GeV/c,$ $ n\sigma_K - shift < 3,$ $0.2 < m^2 < 0.33$	$0.2 < p < 1.6GeV/c,$ $ n\sigma_K - shift < 3,$ $0.16 < m^2 < 0.36;$ $1.6 < p < 2.4GeV/c,$ $ n\sigma_K - shift < 3,$ $0.19 < m^2 < 0.36$	$0.2 < p < 1.2GeV/c,$ $ n\sigma_p - shift < 3;$ $1.2 < p < 4.5GeV/c,$ $ n\sigma_p - shift < 3,$ $0.6 < m^2 < 1.2$
3.9 GeV	$0.2 < p < 0.7GeV/c,$ $ n\sigma_\pi - shift < 3;$ $0.7 < p < 3.0GeV/c,$ $ n\sigma_\pi - shift < 3,$ $-0.1 < m^2 < 0.15$	$0.2 < p < 3.7GeV/c,$ $ n\sigma_\pi - shift < 3$	$0.2 < p < 2.1GeV/c,$ $ n\sigma_K - shift < 3,$ $0.16 < m^2 < 0.36;$ $2.1 < p < 2.6GeV/c,$ $ n\sigma_K - shift < 3,$ $0.2 < m^2 < 0.33$	$0.2 < p < 1.3GeV/c,$ $ n\sigma_K - shift < 3,$ $0.16 < m^2 < 0.36;$ $1.3 < p < 2.1GeV/c,$ $ n\sigma_K - shift < 3,$ $0.19 < m^2 < 0.36$	$0.2 < p < 1.2GeV/c,$ $ n\sigma_p - shift < 3;$ $1.2 < p < 4.5GeV/c,$ $ n\sigma_p - shift < 3,$ $0.6 < m^2 < 1.2$

TABLE VI. PID cut for π, K, p at 3.0, 3.2, 3.5, 3.9 GeV

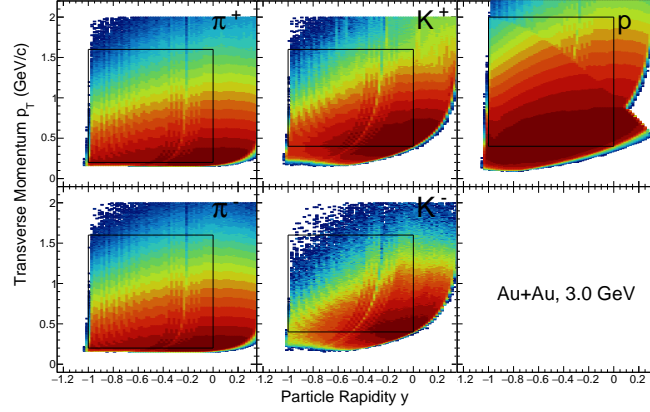


FIG. 34. π, K, p density distribution as function of rapidity and transverse momentum at $\sqrt{s_{NN}} = 3.0$ GeV.

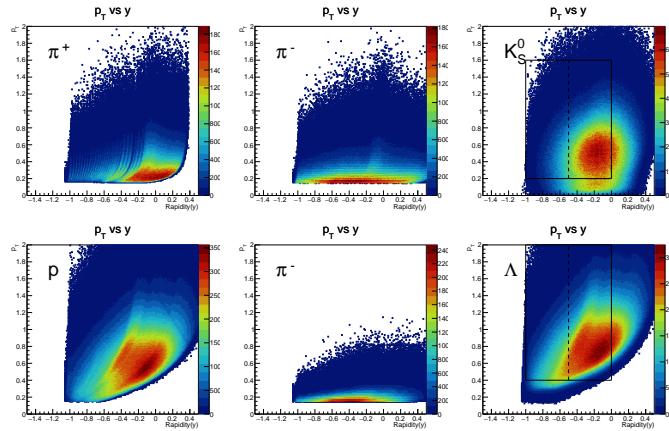


FIG. 35. K_S^0 and Λ (and their daughters) density distribution as function of rapidity and transverse momentum at $\sqrt{s_{NN}} = 3.0$ GeV.

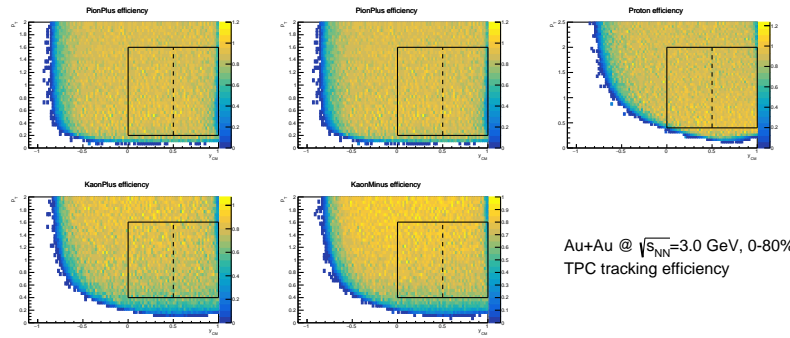


FIG. 36. TPC tracking efficiency of π, K, p as function of rapidity y and transverse momentum p_T at $\sqrt{s_{NN}} = 3.0$ GeV.

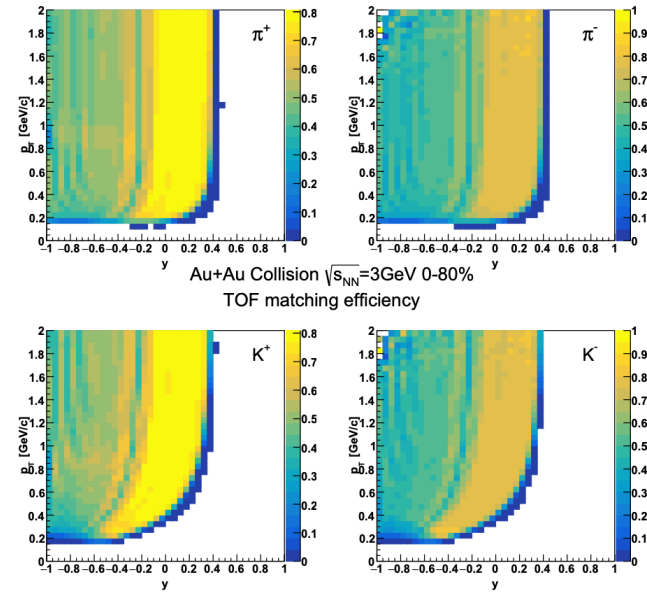


FIG. 37. TOF matching efficiency of π, K as function of rapidity y and transverse momentum p_T at $\sqrt{s_{NN}} = 3.0 \text{ GeV}$.

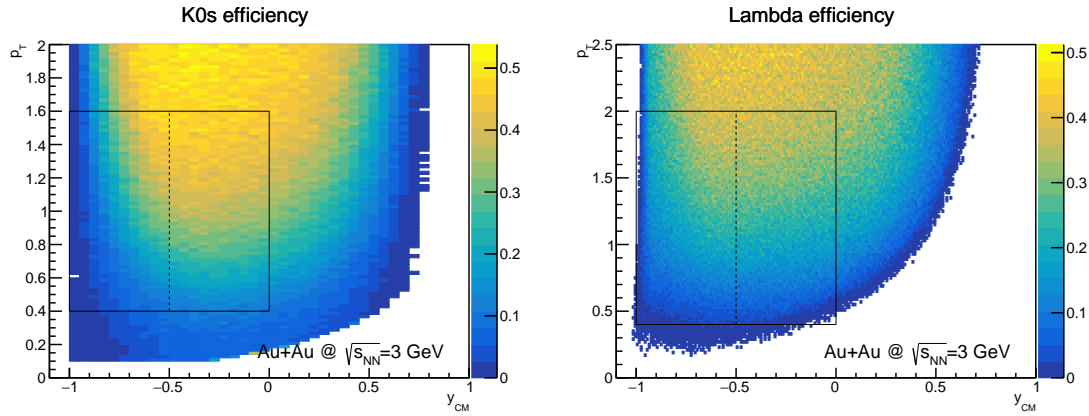


FIG. 38. Reconstruction efficiency of K_S^0 (Left), Λ (Right) as function of rapidity y and transverse momentum p_T at $\sqrt{s_{NN}} = 3.0 \text{ GeV}$.

Appendix A: Appendix

Appendix B: PID cuts and acceptance plots

Appendix C: v_1 plots for other energies

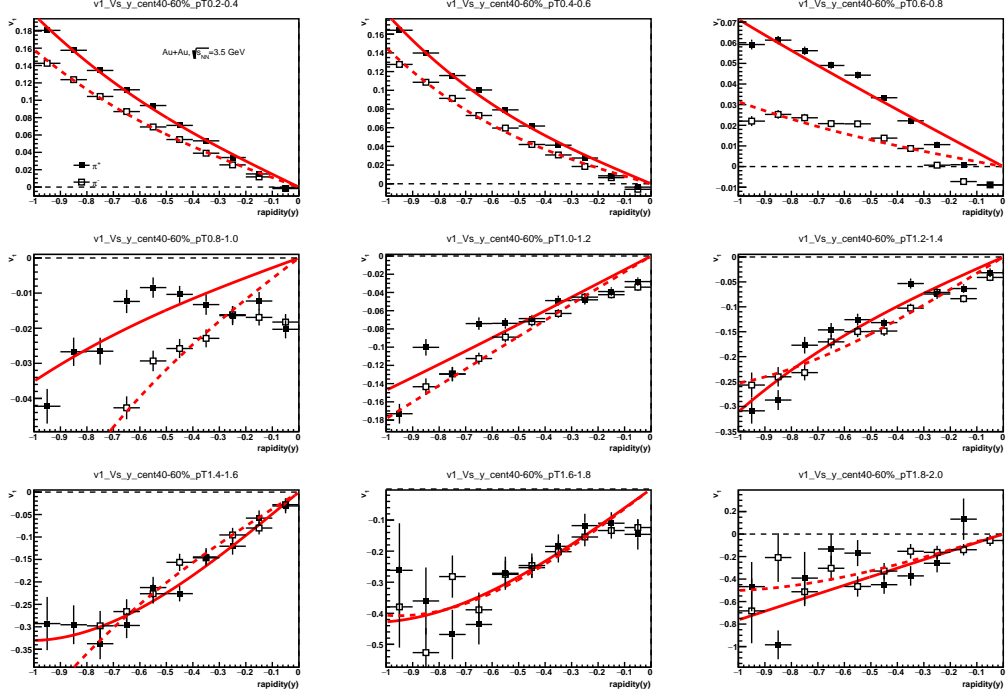


FIG. 39. v_1 of pions as function of rapidity within p_T windows in 40-60% centrality at $\sqrt{s_{NN}} = 3.5$ GeV.

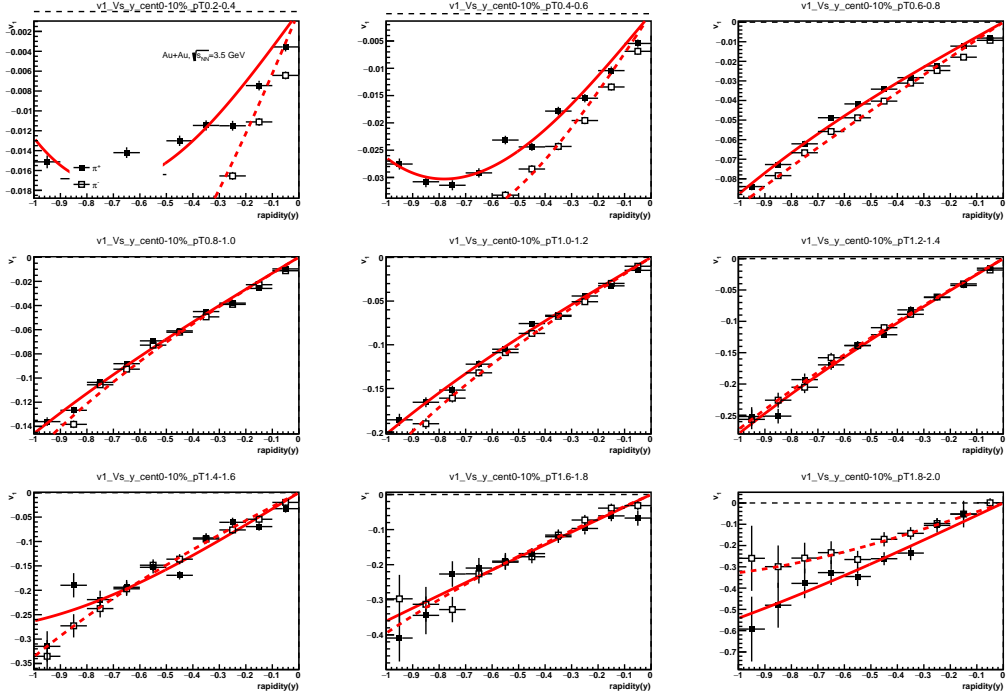


FIG. 40. v_1 of pions as function of rapidity within p_T windows in 0-10% centrality at $\sqrt{s_{NN}} = 3.5$ GeV.

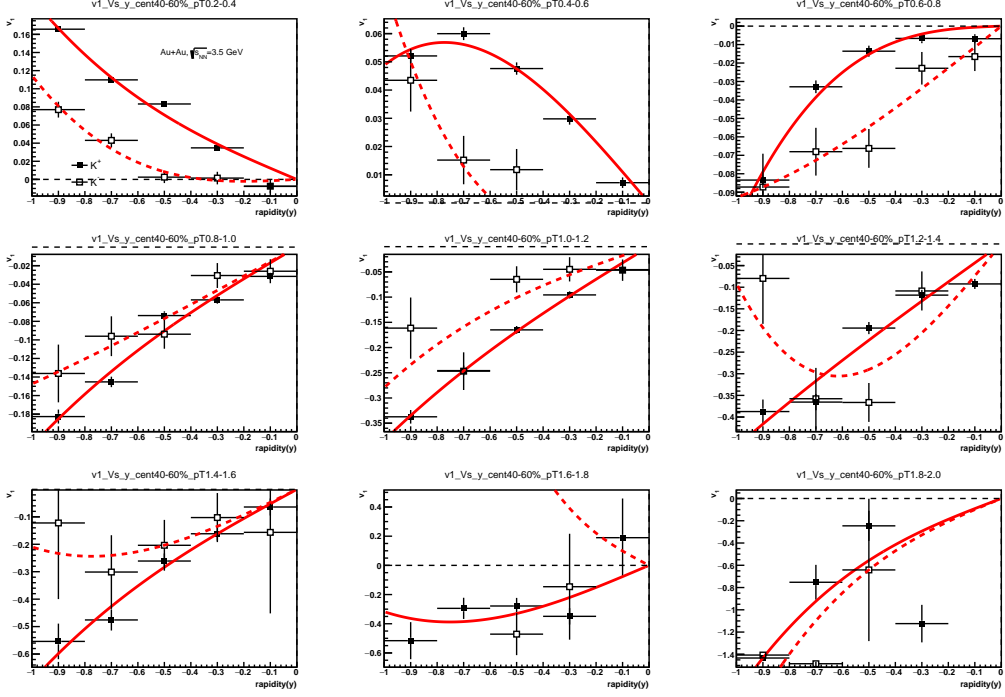


FIG. 41. v_1 of kaons as function of rapidity within p_T windows in 40-60% centrality at $\sqrt{s_{NN}} = 3.5$ GeV.

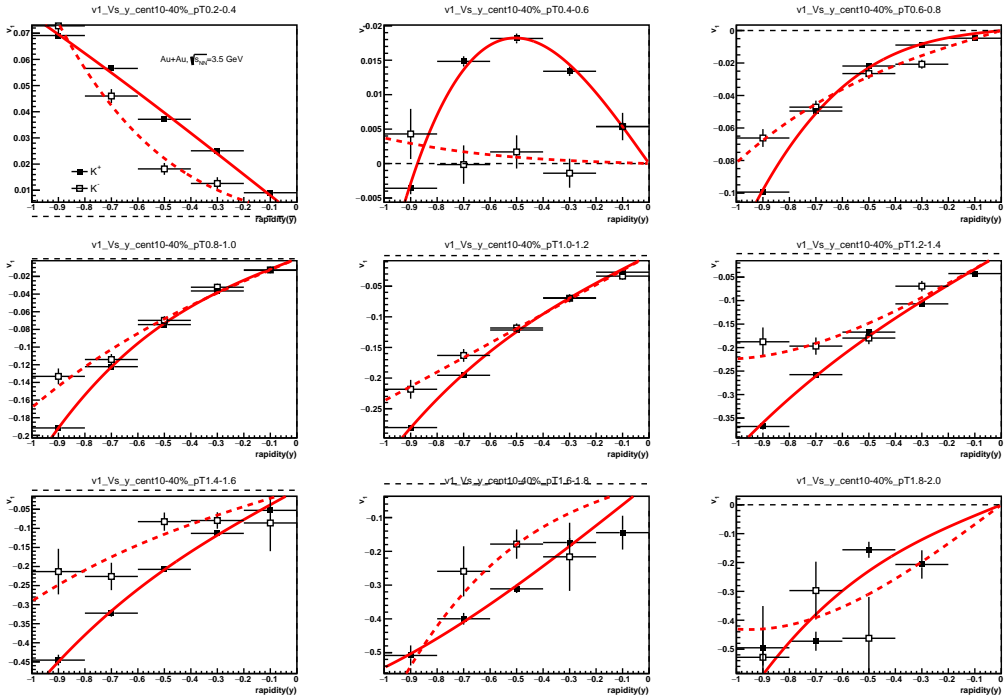


FIG. 42. v_1 of kaons as function of rapidity within p_T windows in 10-40% centrality at $\sqrt{s_{NN}} = 3.5$ GeV.

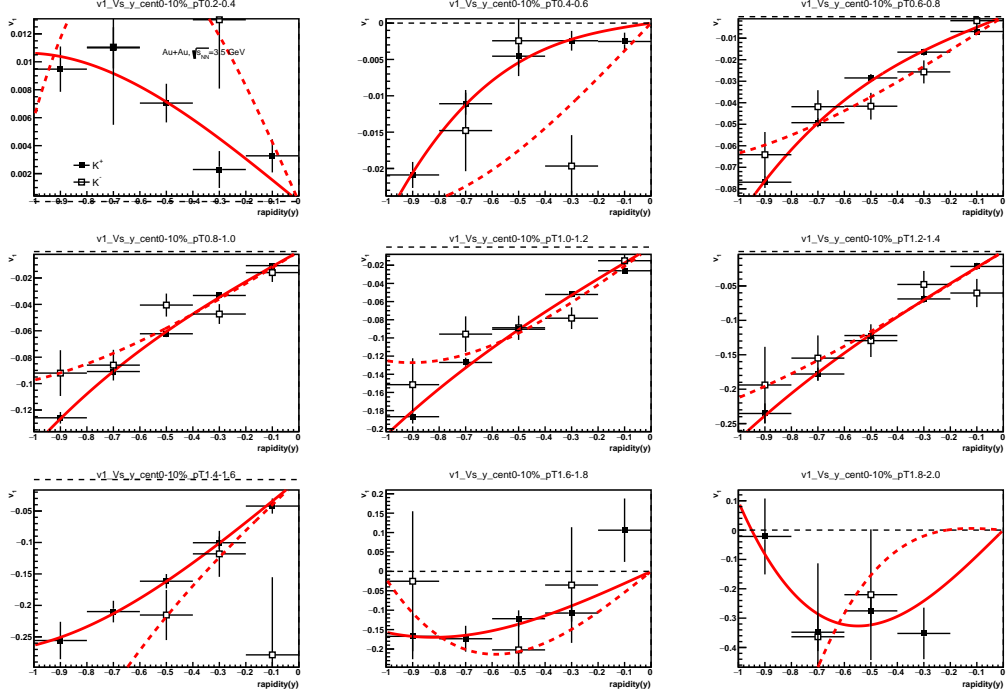


FIG. 43. v_1 of kaons as function of rapidity within p_T windows in 0-10% centrality at $\sqrt{s_{NN}} = 3.5$ GeV.

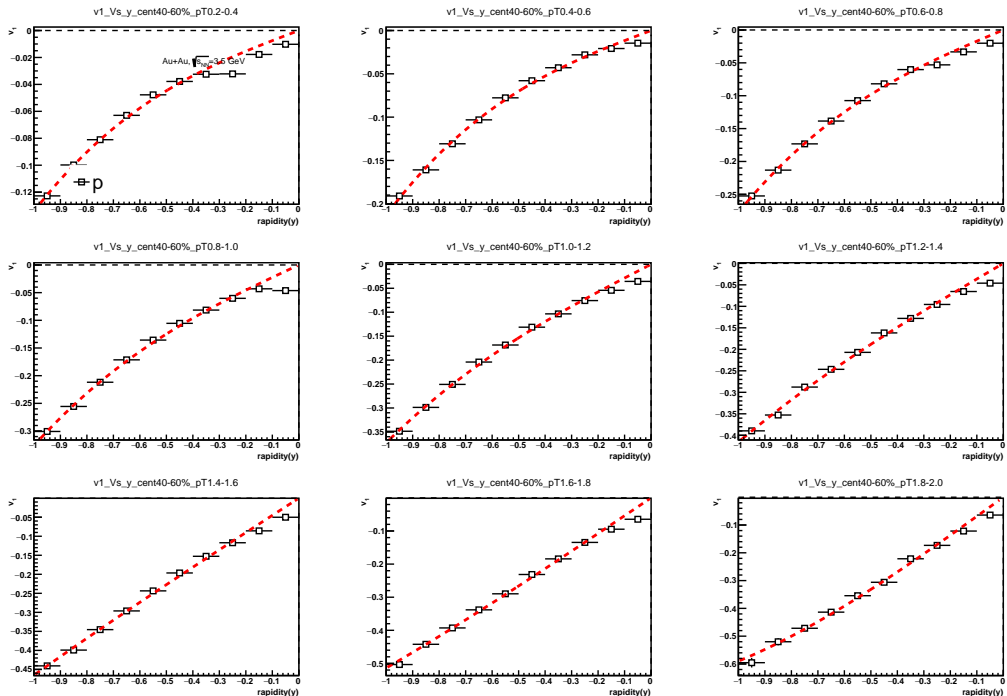


FIG. 44. v_1 of proton as function of rapidity within p_T windows in 40-60% centrality at $\sqrt{s_{NN}} = 3.5$ GeV.

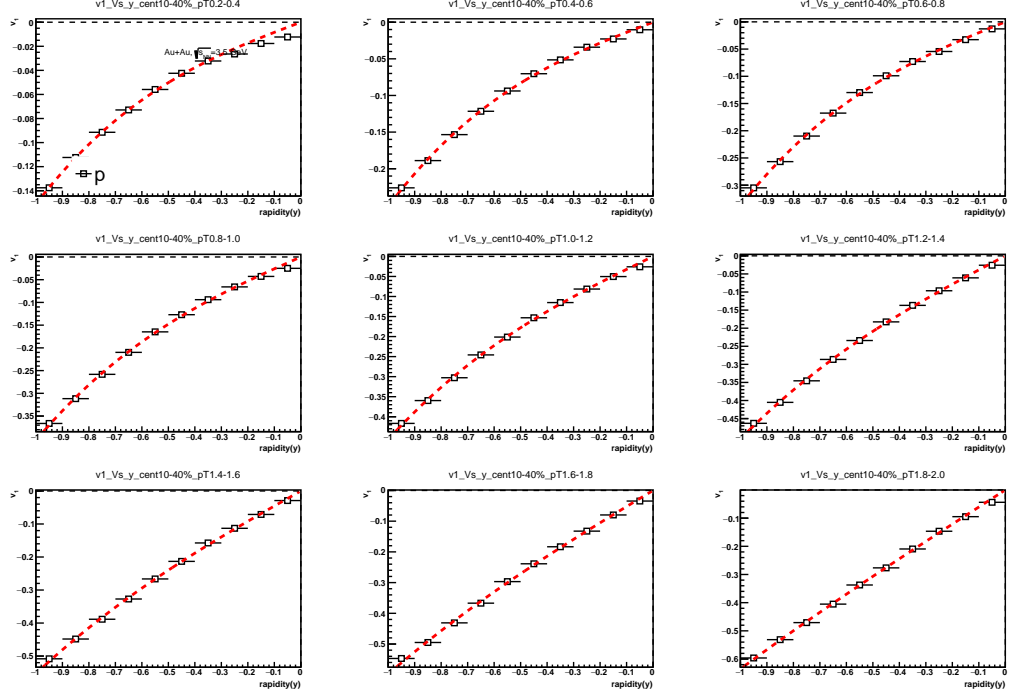


FIG. 45. v_1 of proton as function of rapidity within p_T windows in 10-40% centrality at $\sqrt{s_{NN}} = 3.5$ GeV.

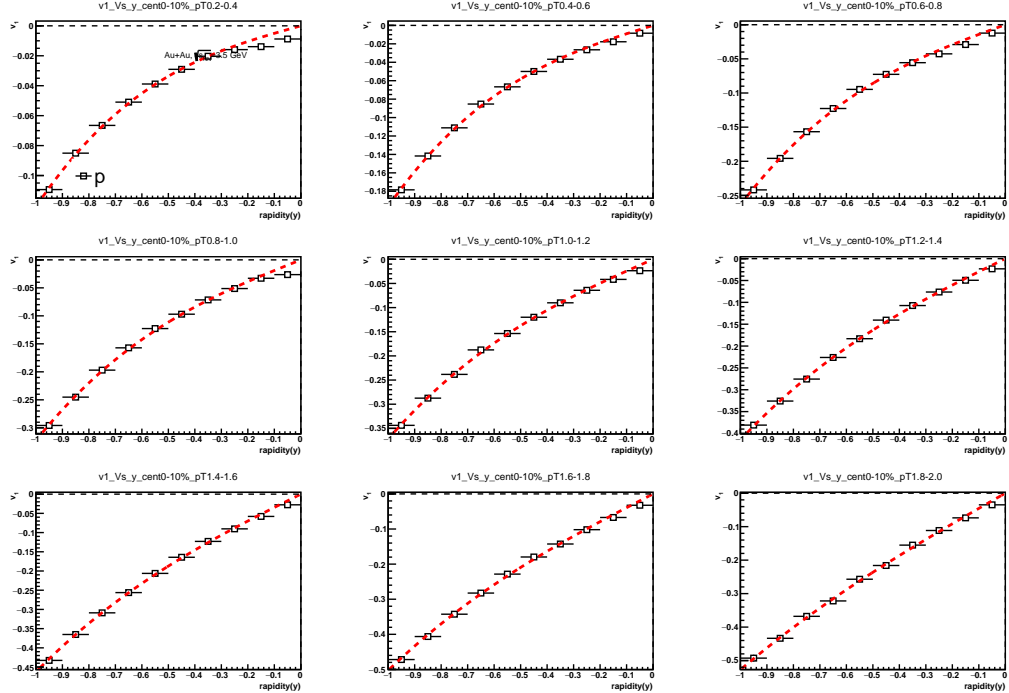


FIG. 46. v_1 of proton as function of rapidity within p_T windows in 0-10% centrality at $\sqrt{s_{NN}} = 3.5$ GeV.

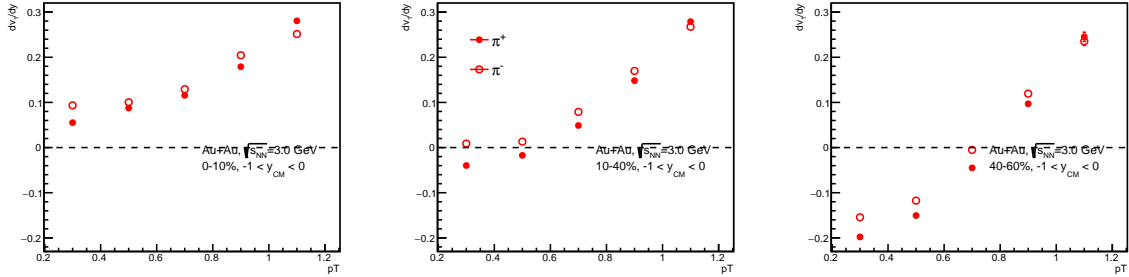


FIG. 47. $dv_1/dy|_{y=0}$ of pions as function of p_T at $\sqrt{s_{NN}} = 3.0$ GeV.

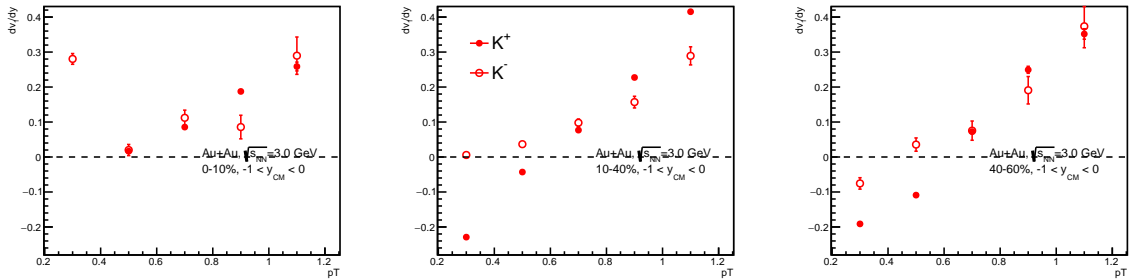


FIG. 48. $dv_1/dy|_{y=0}$ of kaons as function of p_T at $\sqrt{s_{NN}} = 3.0$ GeV.

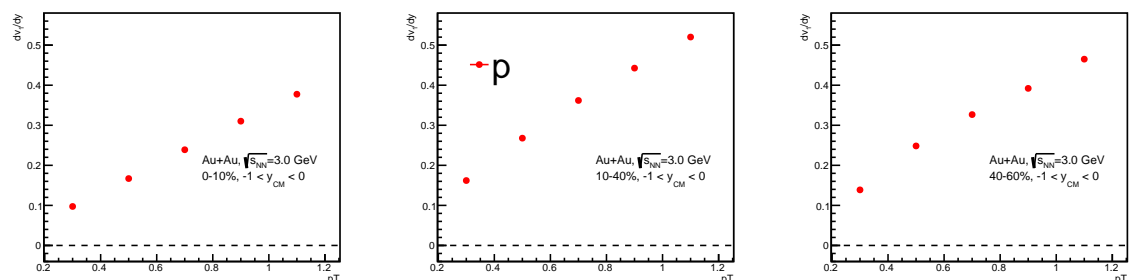


FIG. 49. $dv_1/dy|_{y=0}$ of proton as function of p_T at $\sqrt{s_{NN}} = 3.0$ GeV.

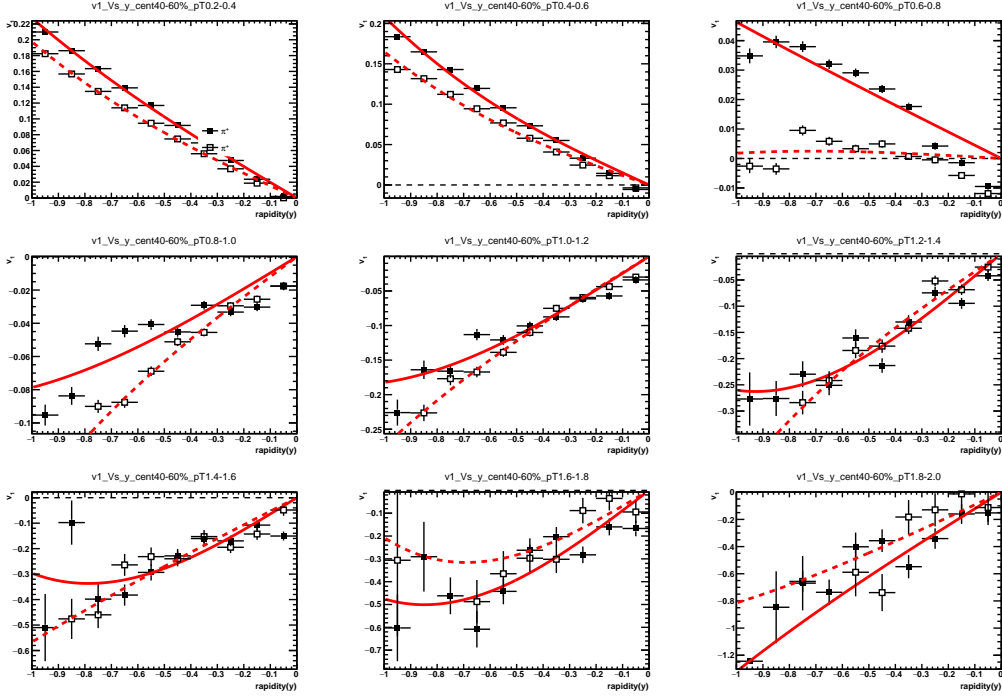


FIG. 50. v_1 of pions as function of rapidity within p_T windows in 40-60% centrality at $\sqrt{s_{NN}} = 3.0$ GeV.

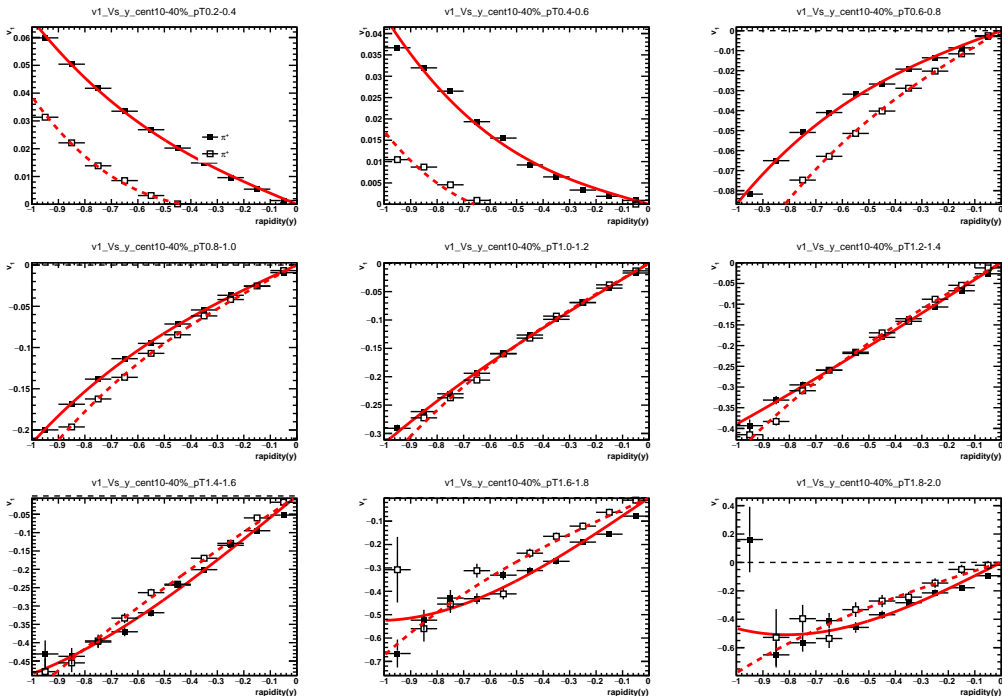


FIG. 51. v_1 of pions as function of rapidity within p_T windows in 10-40% centrality at $\sqrt{s_{NN}} = 3.0$ GeV.

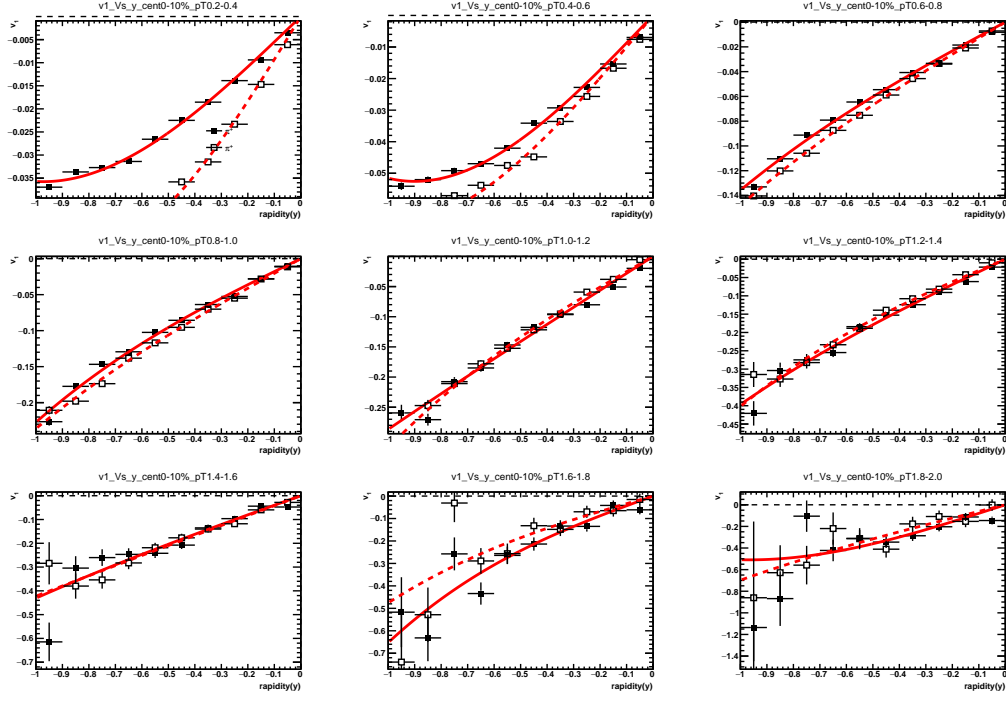


FIG. 52. v_1 of pions as function of rapidity within p_T windows in 0-10% centrality at $\sqrt{s_{NN}} = 3.0$ GeV.

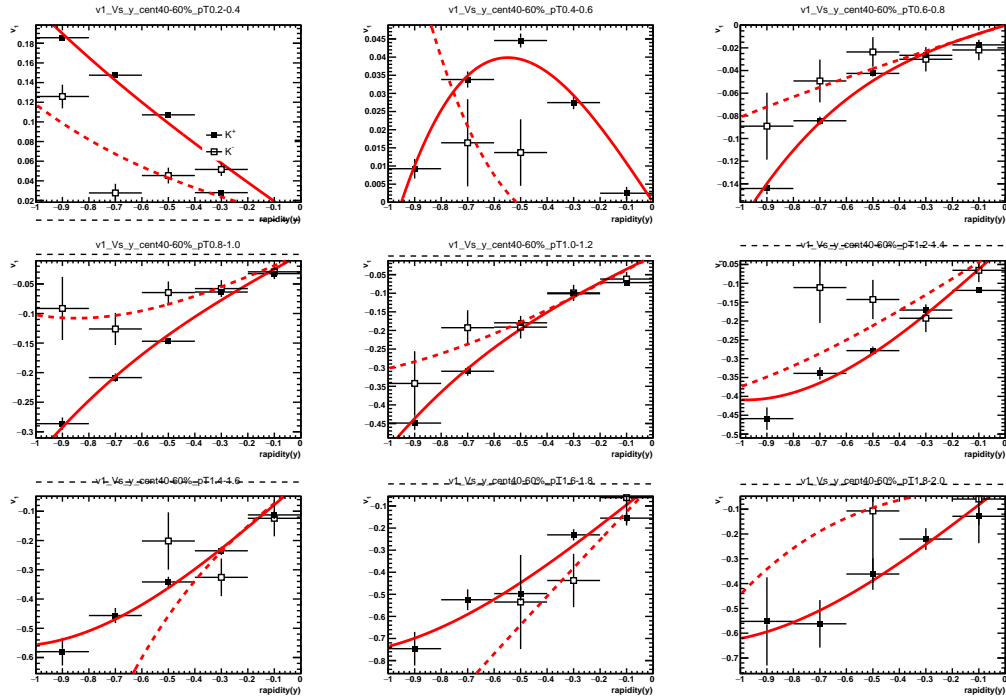


FIG. 53. v_1 of kaons as function of rapidity within p_T windows in 40-60% centrality at $\sqrt{s_{NN}} = 3.0$ GeV.

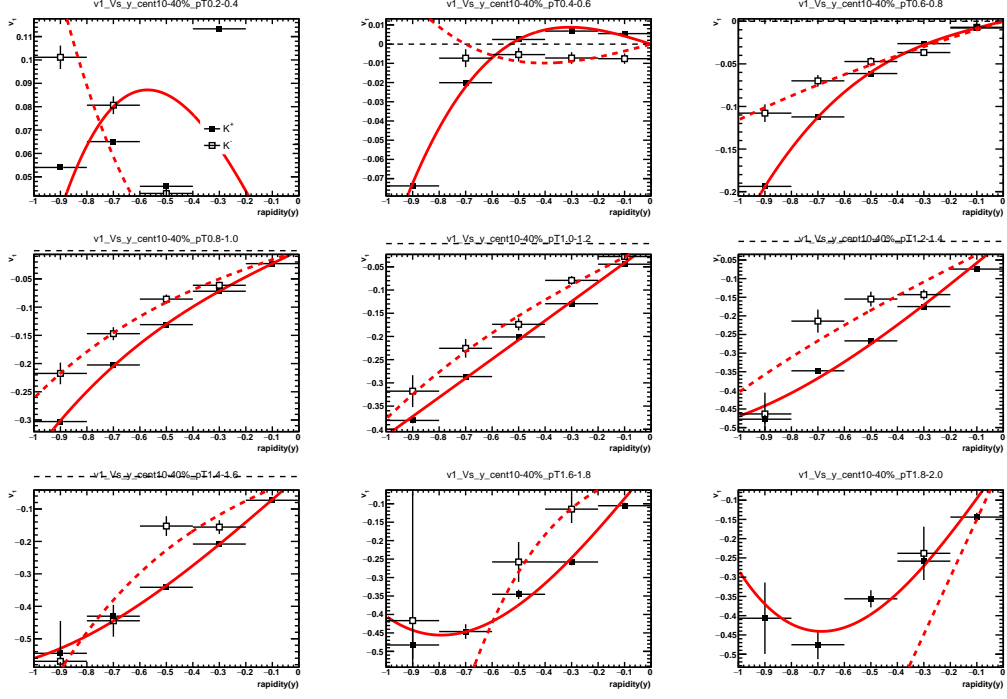


FIG. 54. v_1 of kaons as function of rapidity within p_T windows in 10-40% centrality at $\sqrt{s_{NN}} = 3.0$ GeV.

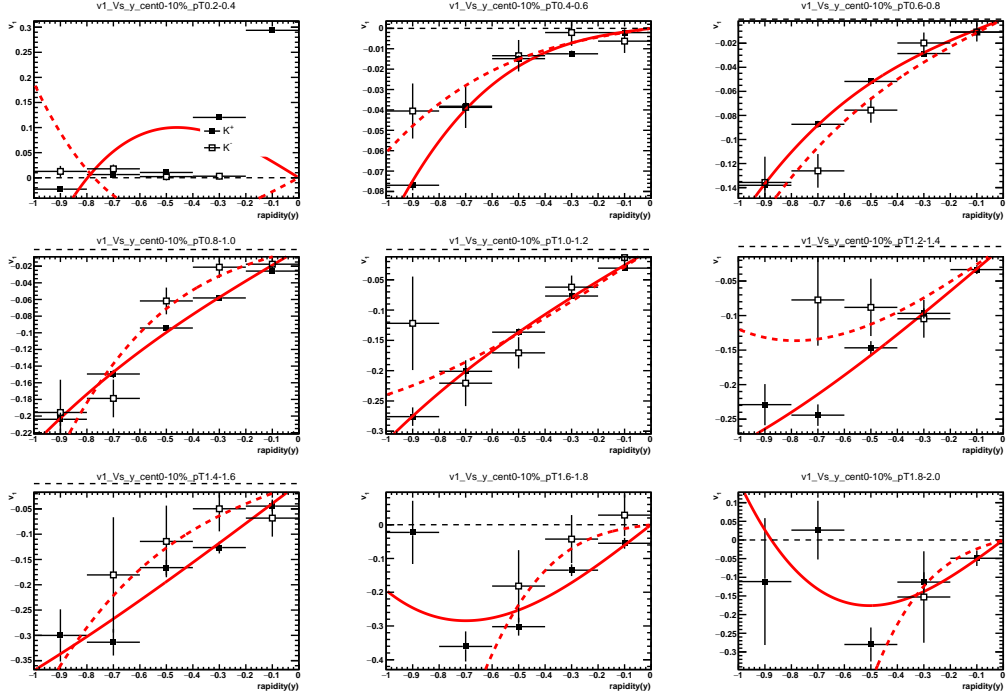


FIG. 55. v_1 of kaons as function of rapidity within p_T windows in 0-10% centrality at $\sqrt{s_{NN}} = 3.0$ GeV.

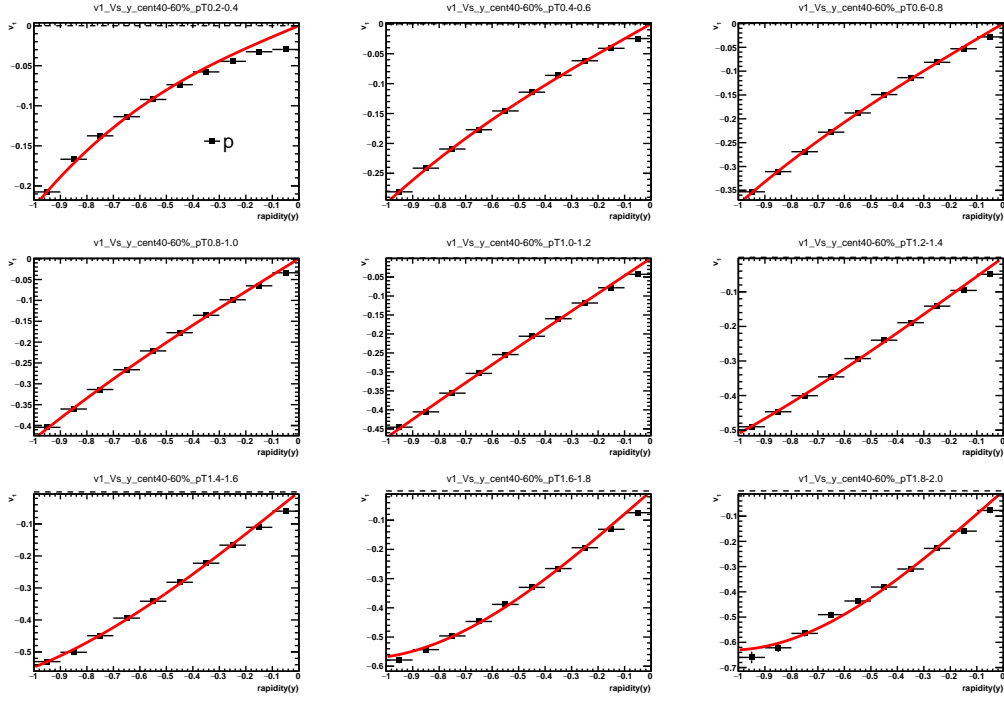


FIG. 56. v_1 of protons as function of rapidity within p_T windows in 40-60% centrality at $\sqrt{s_{NN}} = 3.0$ GeV.

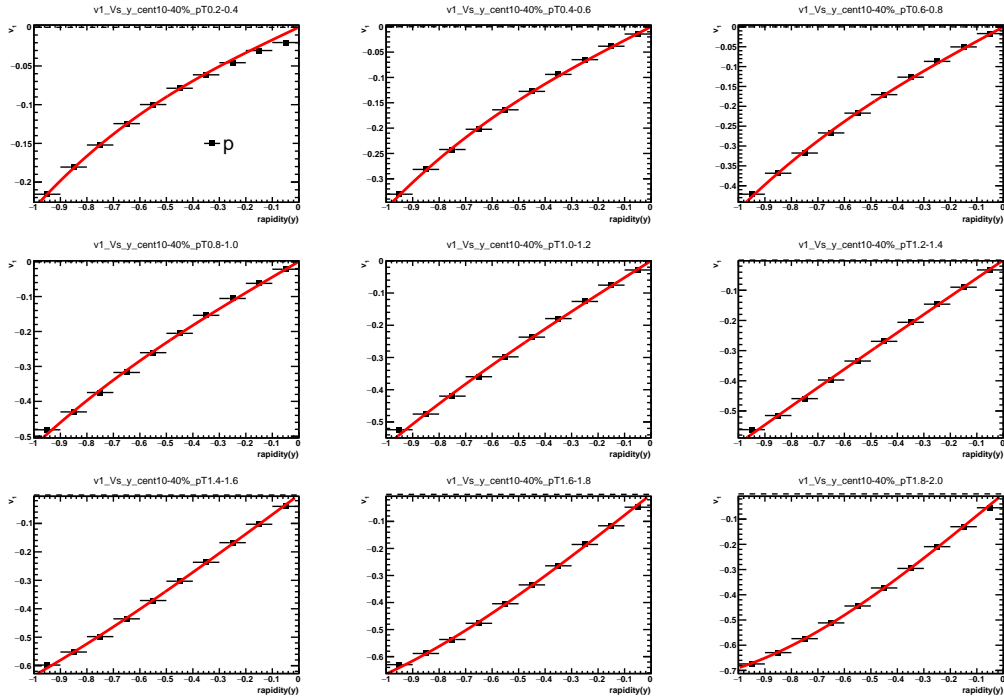


FIG. 57. v_1 of protons as function of rapidity within p_T windows in 10-40% centrality at $\sqrt{s_{NN}} = 3.0$ GeV.

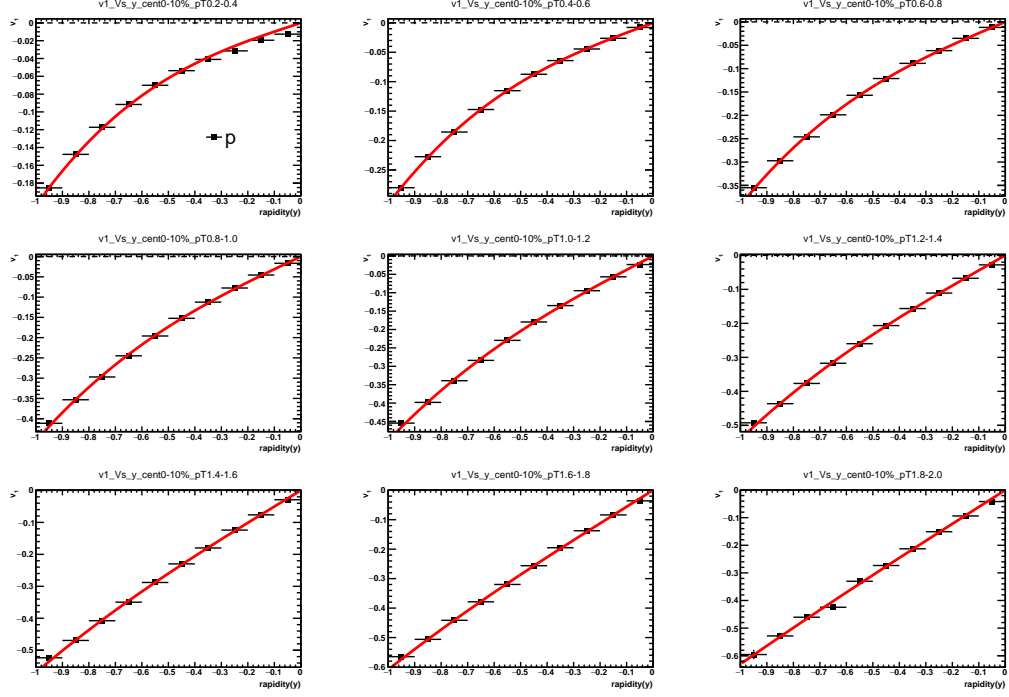


FIG. 58. v_1 of protons as function of rapidity within p_T windows in 0-10% centrality at $\sqrt{s_{NN}} = 3.0$ GeV.

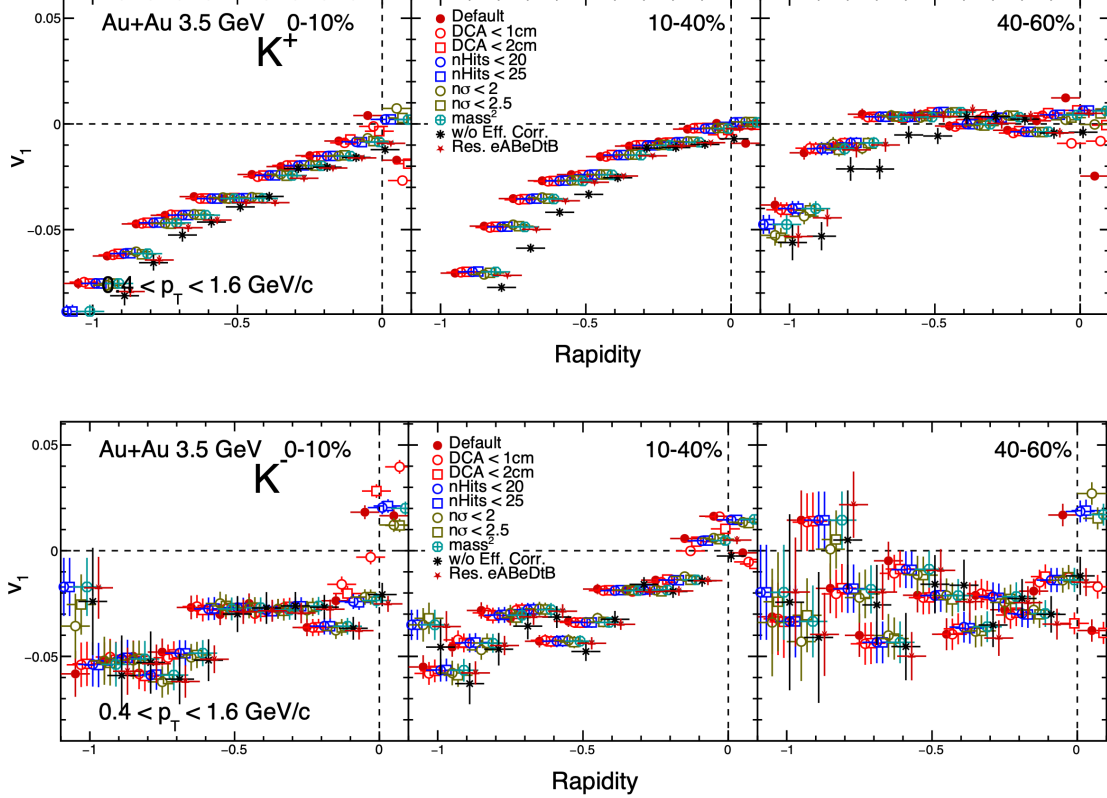


FIG. 59. v_1 of kaons as function of rapidity from systematic sources at $\sqrt{s_{NN}} = 3.5$ GeV.

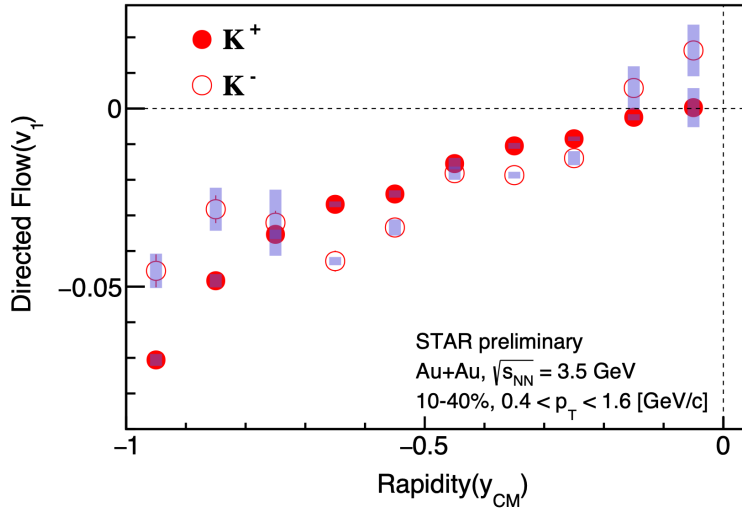


FIG. 60. v_1 of kaons as function of rapidity at $\sqrt{s_{NN}} = 3.5 \text{ GeV}$.

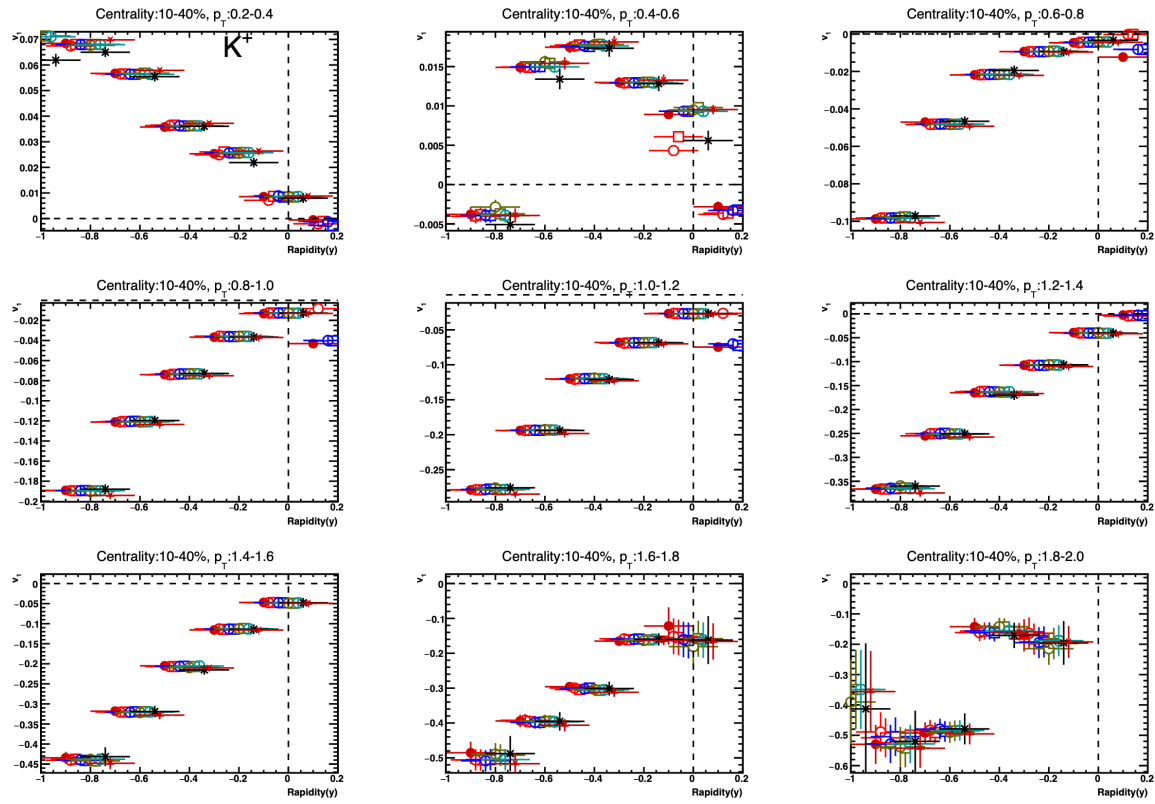


FIG. 61. v_1 of K^+ as function of rapidity within p_T windows at $\sqrt{s_{NN}} = 3.5 \text{ GeV}$.

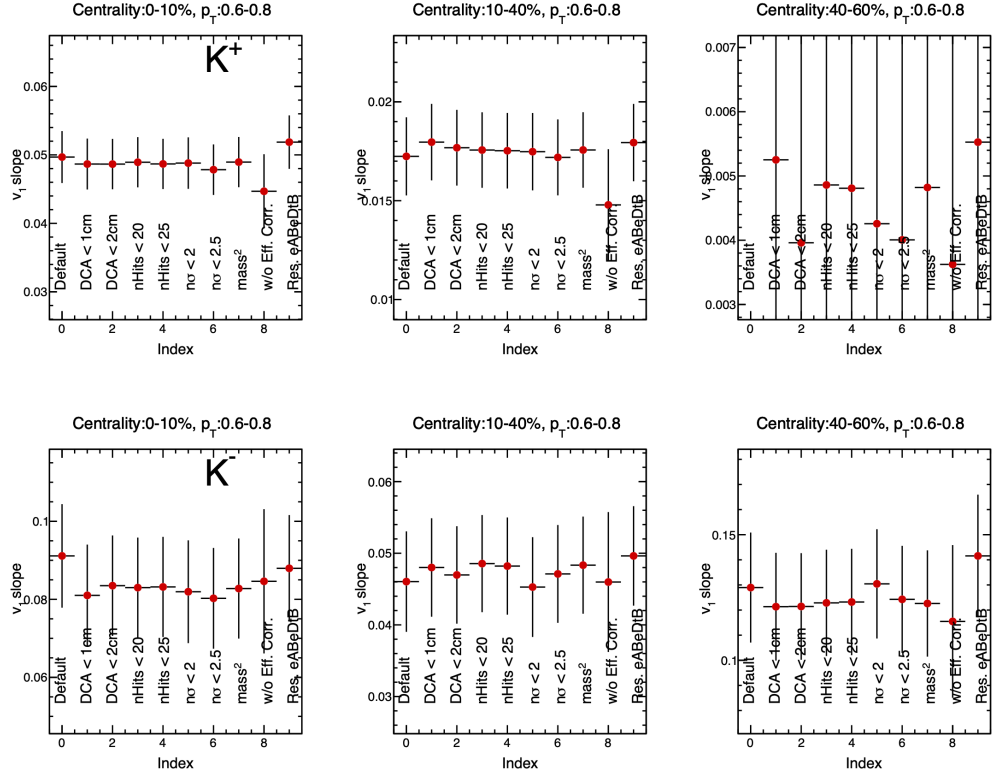


FIG. 62. v_1 slope of kaons as function of systematic sources at $\sqrt{s_{NN}} = 3.5$ GeV.

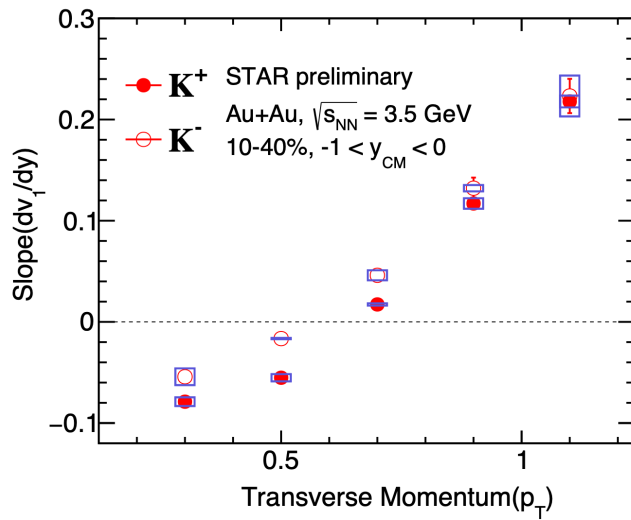


FIG. 63. v_1 slope of kaons as function of transverse momentum at $\sqrt{s_{NN}} = 3.5$ GeV.

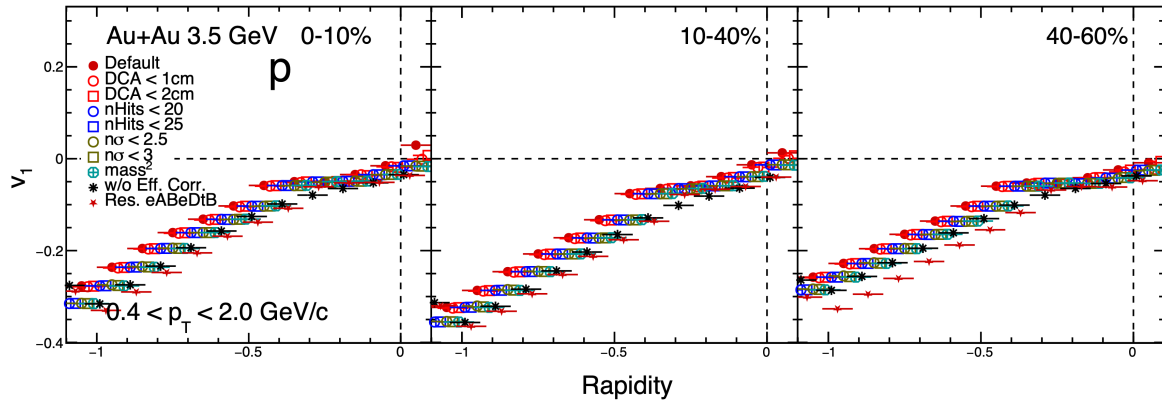


FIG. 64. v_1 of proton as function of rapidity from systematic sources at $\sqrt{s_{NN}} = 3.5$ GeV.

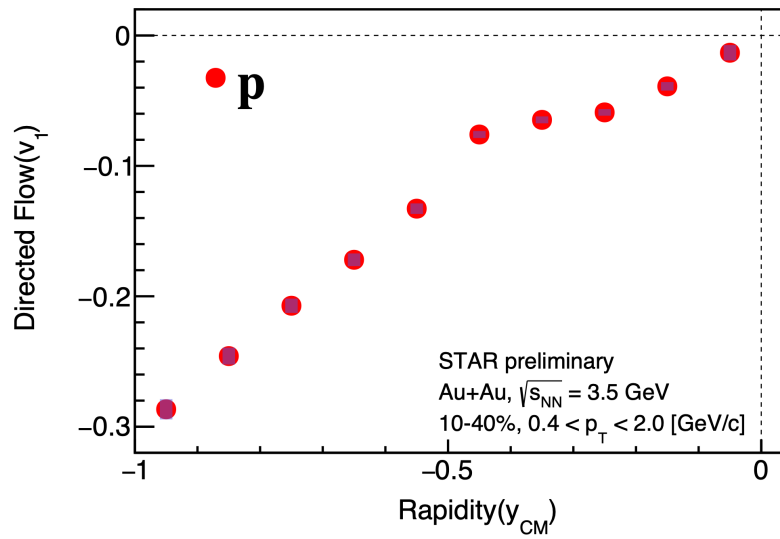
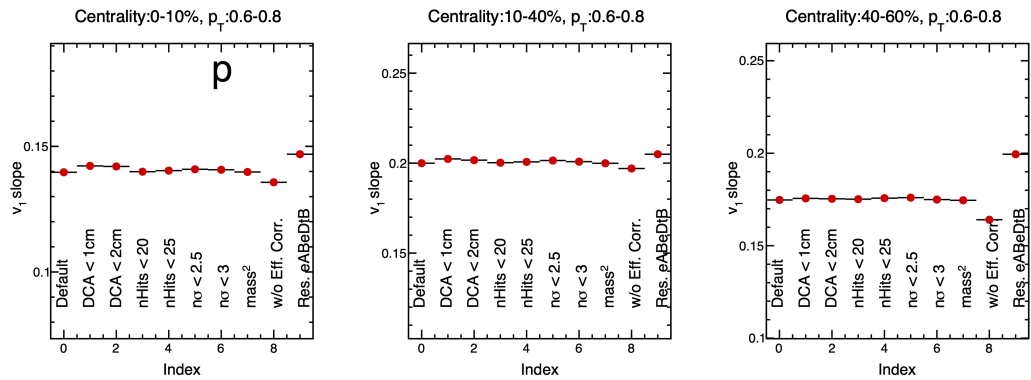
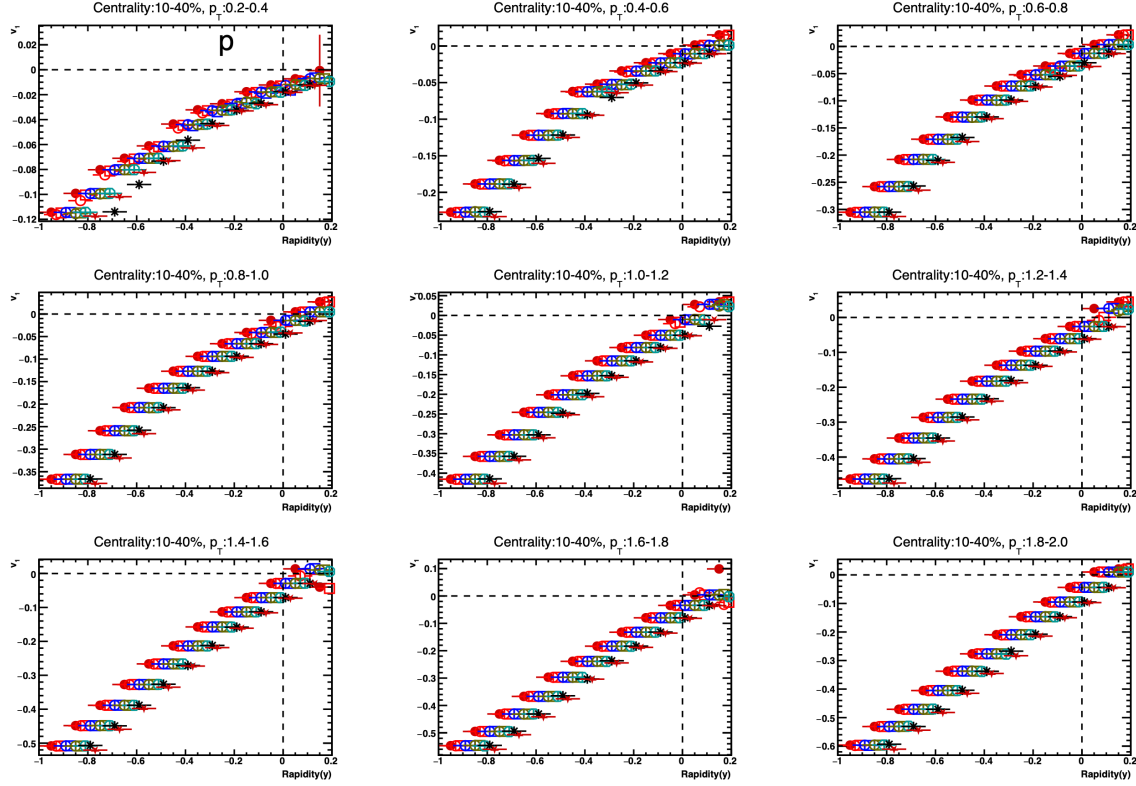


FIG. 65. v_1 of proton as function of rapidity at $\sqrt{s_{NN}} = 3.5$ GeV.



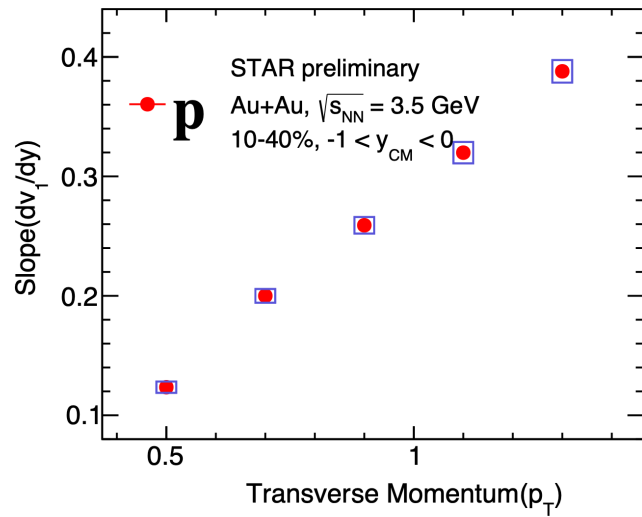


FIG. 68. v_1 slope of proton as function of transverse momentum at $\sqrt{s_{NN}} = 3.5 \text{ GeV}$.

-
- [1] M. S. Abdallah *et al.* (STAR Collaboration), *Phys. Rev. C* **103**, 034908 (2021).
 - [2] D. Kharzeev and M. Nardi, *Physics Letters B* **507**, 121 (2001).
 - [3] A. Bilandzic, R. Snellings, and S. Voloshin, *Phys. Rev. C* **83**, 044913 (2011).
 - [4] J. Adams *et al.*, *Nuclear Instruments and Methods in Physics Research Section A: Accelerators, Spectrometers, Detectors and Associated Equipment* **968**, 163970 (2020).
 - [5] S. A. Voloshin, A. M. Poskanzer, and R. Snellings, “Collective phenomena in non-central nuclear collisions,” (2008), [arXiv:0809.2949 \[nucl-ex\]](https://arxiv.org/abs/0809.2949).
 - [6] A. M. Poskanzer and S. A. Voloshin, “Methods for analyzing anisotropic flow in relativistic nuclear collisions,” (1998), [arXiv:nucl-ex/9805001 \[nucl-ex\]](https://arxiv.org/abs/nucl-ex/9805001).
 - [7] M. Abdallah *et al.* (STAR Collaboration), *Physics Letters B* **827**, 137003 (2022).
 - [8] M. Anderson *et al.*, *Nuclear Instruments and Methods in Physics Research Section A: Accelerators, Spectrometers, Detectors and Associated Equipment* **499**, 659 (2003), the Relativistic Heavy Ion Collider Project: RHIC and its Detectors.
 - [9] W. Llope, *Nuclear Instruments and Methods in Physics Research Section A: Accelerators, Spectrometers, Detectors and Associated Equipment* **661**, S110 (2012), x. Workshop on Resistive Plate Chambers and Related Detectors (RPC 2010).
 - [10] A. Banerjee, I. Kisel, and M. Zyzak, *International Journal of Modern Physics A* **35**, 2043003 (2020).
 - [11] S. Agostinelli *et al.*, *Nuclear Instruments and Methods in Physics Research Section A: Accelerators, Spectrometers, Detectors and Associated Equipment* **506**, 250 (2003).
 - [12] R. Barlow, “Systematic errors: facts and fictions,” (2002), [arXiv:hep-ex/0207026 \[hep-ex\]](https://arxiv.org/abs/hep-ex/0207026).